# AN ABSTRACT OF THE THESIS OF

Gable D. Roth for the degree of Master of Science in Nuclear Engineering presented on June 6<sup>th</sup> 2011

 Title: CFD Analysis of Pressure Differentials in a Plate-Type Fuel Assembly

Abstract approved:

_____

Brian G. Woods

The Hydro-Mechanical Fuel Test Facility (HMFTF) is being built at Oregon State University to evaluate fluid flow through plate-type fuel assemblies. The first plate assembly that will be examined in the facility is the Generic Test Plate Assembly (GTPA). The GTPA consists of an array of six parallel flat plates, 24 inches long, forming seven flow channels. The plates are a total of 4 inches wide and 0.05 inches thick with 0.25 inches of the plate edge being imbedded in the side plate making a flow channel of 3.5 inches wide. The height of the flow channels is adjustable. A support comb is used to stiffen the free edges of the fuel plates.

The Star-CCM+ CFD tool was used to analyze fluid flow through the GTPA with channels of equal height (0.075 inches) except for the middle channel which was 0.125 inches high. Using standard CFD practices the mesh type, mesh size, and turbulence model were selected. Using different boundary conditions, consisting of three flow rates with a fixed temperature and three temperatures, with the flow rate fixed at one of the three analyzed flow rates, the pressure differentials between the channels were analyzed to determine the possibility of plate deflection.

The analysis revealed that the pressure difference between the channels increased with increasing volumetric flow rate. The results also indicate that as the system temperature increased the pressure differential between the channels decreased slightly. Velocity results were compared to Miller's critical velocity and indicate that plate deflection is not expected to occur at the inlet of the channel due to the stiffening caused by the presence of the support comb.

CFD Analysis of Pressure Differentials in a Plate-type Fuel Assembly

by

Gable D. Roth

A THESIS

submitted to

Oregon State University

in partial fulfillment of

the requirements for the

degree of

Master of Science

Presented June 6, 2011

Commencement June 2012

Master of Science thesis of Gable D. Roth presented on June 6, 2011.

APPROVED:

_____

Major Professor, representing Nuclear Engineering

_____

Head of the Department of Nuclear Engineering and Radiation Health Physics

_____

Dean of the Graduate School

I understand that my thesis will become part of the permanent collection of Oregon State University libraries. My signature below authorizes release of my thesis to any reader upon request.

_____

Gable D. Roth, Author

# TABLE OF CONTENTS

Table of Contents (Continued)

Table of Contents (Continued)

# LIST OF FIGURES

LIST OF FIGURES (Continued)

LIST OF FIGURES (Continued)

# LIST OF TABLES

# Nomenclature

**Symbols**

| | |
|---|---|
| $a$ | Plate thickness |
| $b$ | Plate width |
| $g$ | Gravitational acceleration |
| $h$ | Initial flow channel height at midspan |
| $l$ | Effective plate length |
| $\dot{m}$ | Mass flow rate |
| $p$ | Pressure difference required to cause plate to bend |
| $r$ | Ratio of cell count |
| $v_f$ | Volume fraction of fuel foil |
| $v_m$ | Volume fraction of matrix |
| $x$ | Longitudinal distance from edge support |
| $y$ | Deflection of plate relative to edge supports |
| $z$ | Order of solution |
| $E$ | Young's Modulus |
| $E_f$ | Young's Modulus for fuel foil |
| $E_m$ | Young's Modulus for matrix |
| $E_T$ | Total Young's Modulus for matrix and fuel foil |
| $I$ | Area moment of inertia of plate |
| $Q$ | Volumetric flow rate |
| $S$ | Original cross-sectional area of flow channel |
| $\Delta S$ | Change in $S$ |

**Symbols**

$V_0$             Linear velocity of coolant

$V_{cr}$           The velocity required to cause a plate to buckle

$\varepsilon$             Uncertainty value

$\varphi_1$            Solution generated using fine mesh

$\varphi_2$            Solution generated using coarse mesh

$\rho$             Density of coolant

$v$             Poisson's ratio of plate

$\Phi$             Richardson's extrapolated value

# CFD Analysis of Pressure Differentials in a Plate-type Fuel Assembly

## 1   INTRODUCTION

According to the International Atomic Energy Association (IAEA), as of 2009 there are 41 operating research and test reactors in the United States [1]. These research facilities are utilized in countless ways to provide technical assistance in all engineering disciplines and as such, are all unique in design. One aspect of their individuality may be seen in the fuel geometry each reactor employs. While traditional light water power reactors (and most research reactors) use rod type fuel, a number of facilities use plate-type fuel. Plate-type fuel is potentially advantageous for numerous reasons including:

- An increase in kinetic efficiency (optimized moderator to fuel ratio)
- An increase in thermal neutron flux
- An increase in power density

There are also a number of possible disadvantages to this type of fuel:

- It requires high precision and a significant increase in fabrication resources
- It has an inherently faster burn-up rate resulting in shorter core lifetimes
- Its plates are prone to deflection

## 1.1   Background

The Hydro-Mechanical Fuel Test Facility (HMFTF), located at Oregon State University (OSU) is a thermal hydraulic separate effects test loop. This facility was originally designed to provide supplemental data for the qualification of low enriched uranium (LEU) fuel for the five high performance research reactors in the U.S. (USHPRR).

In order to maintain the high performance capabilities of these reactors the fuel that is used in the conversion process needs to have a higher uranium density than the fuel that is currently in use. Currently these reactors employ a dispersion fuel consisting of

a U-Al$_x$ alloy suspended in a 6061-0 aluminum matrix. The fuel proposed for conversion is a U-Mo monolithic fuel. Monolithic fuel consists of a thin sheet of fuel foil being placed in the center of nonfissionable material. The matrix material for the proposed U-Mo monolithic fuel is also 6061-0 aluminum. A visual representation of each type of fuel is shown in Figure 1.1.

Dispersion Fuel Cross-Sectional View    Cladding    Monolithic Fuel Cross-Sectional View

Fuel Foil
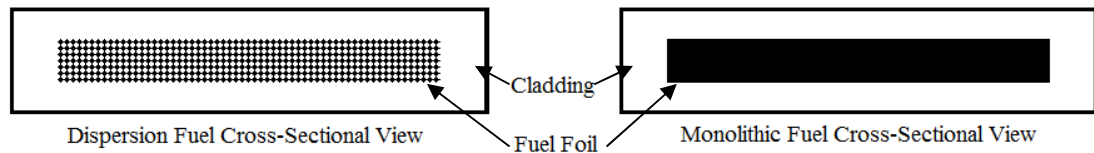
Figure 1.1: Comparison of dispersion and monolithic fuel types

Testing in the HMFTF is planned to be broken into two phases. The first phase is identified as *fuel qualification testing*. These tests will provide a qualitative demonstration that mechanical stability of USHPRR fuel plates will not be compromised due to a change in fuel foil composition. Phase one testing will be done using a generic fuel form – a Generic Test Plate Assembly (GTPA), to collect data and compare the relative mechanical performance of all fuel compositions considered during this study. Phase two – *Reactor Specific Testing*; will then focus on reactor-specific assembly tests, as required for each USHPRR's conversion Safety Analysis Report (cSAR) [2].

As part of the first phase, this study focuses on the GTPA. Typically, fuel assembly channel gaps (the gap between fuel plates in an array of fuel plates) are sized to prevent fuel plate deformation in normal thermal hydraulic conditions in the reactor. Bench top testing has indicated that U-Mo monolithic fuel is at least as robust as the currently used U-Al$_x$ dispersion fuel through the demonstration of increased modulus of elasticity [2]. However, comparison testing at elevated temperatures and flow rates is desired to demonstrate the U-Mo's structural performance up to and beyond measurable plastic deformation.

Testing will be done using a specially designed modular GTPA to compare performance of three types of plates: U-Mo monolithic, U-Al$_x$ dispersion, and Al. Depleted Uranium (DU) will be used in place of the uranium for the U-Mo test plates, and a stainless steel surrogate will be used in place of the uranium for the U-Al$_x$ plates. DU differs from enriched uranium and natural uranium on the atomic level only. Since the tests conducted in this facility are not dependent upon the atomic structure of the material, DU can be easily used in place of the enriched uranium. The stainless steel surrogate was chosen to be used for the dispersion fuel because of limited resources making the use of DU in a dispersion fuel more difficult.

The safety analysis report (SAR) for the Advance Test Reactor (ATR) provides data from experiments conducted on these material types. The results indicate that the U-Al$_x$ dispersion fuel has higher yield strength than the 6061-0 aluminum cladding [3]. This indicates that a plate tested using pure 6061-0 aluminum cladding would buckle sooner than a plate containing U-Al$_x$ dispersion fuel resulting in a conservative estimate of plate buckling. The material properties of the U-Mo monolithic fuel can be analyzed analytically. This analytical analysis is presented in Section 4.3.7 and helps to give an idea as to how the 6061-0 aluminum plate would compare to the U-Mo monolithic plate experimentally.

To test the limits of test plate performance at elevated temperatures and flow rates, the GTPA has been designed to accommodate varying channel gap widths. These differences will result in pressure differentials across corresponding test plates; plastic deformation of these plates occurs when pressure differentials exceed the plate's yield stress. The GTPA is designed such that the yield stress is exceeded near the maximum test temperature and flow rate bound by the operational limits of the HMFTF [4]. The GTPA frame is designed with versatility, allowing the channel gaps to be varied so a range of channel gaps can be evaluated if necessary. The GTPA design is modular, so

the test plates can be assembled into the complete GTPA prior to each test and disassembled at the conclusion of each test. By designing the GTPA in such a modular manner, its frame may be used for all of the test plate-types, reducing the number of mechanical components requiring fabrication. Support combs, or plate combs, are inserted between the plates at the inlet and the outlet of the channels. A diagram of the comb is shown in Figure 1.2.
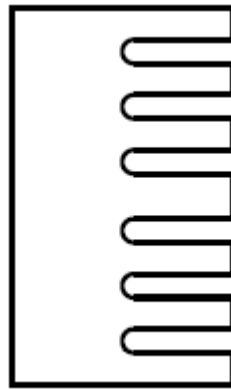
Figure 1.2: Support comb

The comb will limit the maximum plate deflection to take place in the middle of the plates instead of at the inlet and outlet. The comb is inserted into each channel at the center of the plate width. The GTPA is designed to use this support comb when needed [4]. Figure 1.3 shows an image of the GTPA with the associated dimensions (Figure taken from Reference [4]).
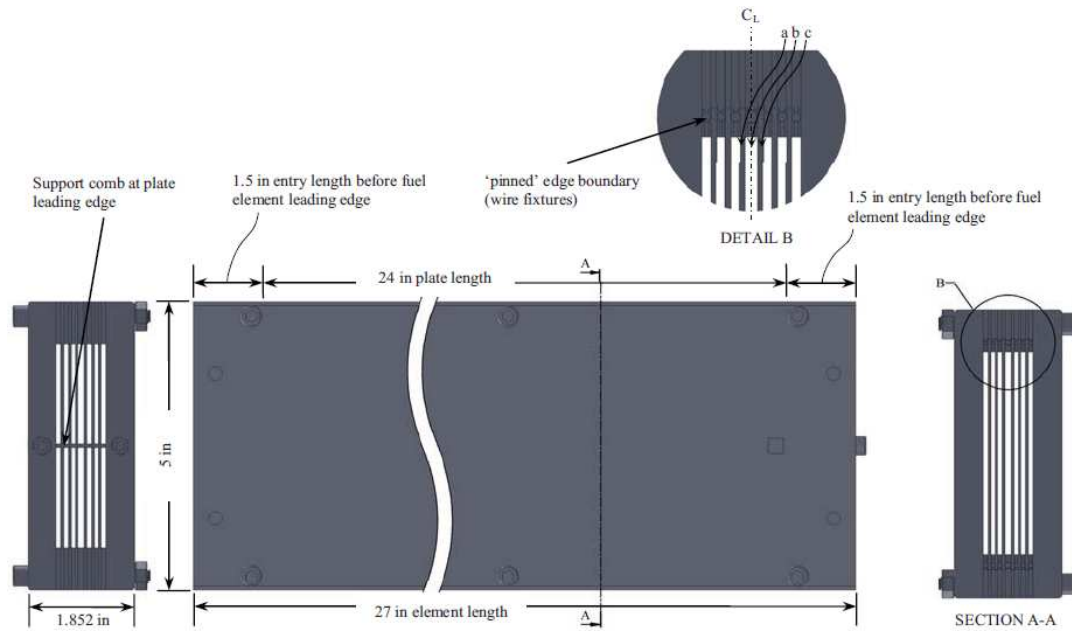
Figure 1.3: Geometric layout of the GTPA

The distance in between fuel plates is larger in the center channel than it is in the other six channels. This distance will be referred to as the channel height and is 0.125 inches for the center channel and 0.075 inches for the other six channels. The distance between the channel side supports is 3.5 inches and will be referred to as the channel width or span-width. The distance from the inlet to the outlet of the assembly is 27 inches and the total length of the fuel plate is 24 inches providing a 1.5 inch mixing region at the inlet and the outlet of the assembly.

Computational Fluid Dynamics (CFD) techniques are often utilized during an experimental study prior to collecting any data in order to confirm the study's initial hypotheses and justify the experimental design itself. CFD codes have been used for many years in fuel assembly analyses. Prior to tests conducted in the HMFTF, CFD simulations will be used to predict the plate deflection of the GTPA by studying the pressure differentials within the channels.

## 1.2  Objective

The objective of the work presented herein is first to analyze various boundary conditions to determine the associated pressure differentials within the GTPA using the CFD tool Star-CCM+ version 5.04.008. Second, this data will be used to determine how great the risk is of plate deflection under these same conditions within the HMFTF. When the GTPA is tested experimentally the data collected from those experiments will be used to verify the results produced in this analysis.

## 1.3  Importance

The results of this work will help to determine the possibility of plastic deflection for the HPRR fuel assemblies with the new low enriched fuel under standard operating conditions.

## 1.4  Assumptions

Star-CCM+ version 5.04.008 is a program that uses CFD to model fluid flow. There are many assumptions that need to be made in order to develop the best possible model of a flow scenario. A brief description of several assumptions is presented in the sections that follow.

### 1.4.1  One Channel

- Although this is a simplified model that does not include all features of the actual geometry it is assumed that this model will be sufficient for the selection of mesh type, mesh refinement, turbulence model, physics models, initial conditions, and boundary conditions.

- There is no entry length for this model; mixing in the inlet and exit region is assumed to be insignificant.

- Due to the high velocity and pressure within the channel the effects on the flow resulting from gravity are minimal and are not modeled in the simulation.

### *1.4.2  Two Channel Model*

- It is assumed that the entry region prior to channel separation is sufficient in length to produce a fully developed flow suitable for an accurate representation of operational flow.

- Due to the high velocity and pressure within the channel the effects on the flow resulting from gravity are minimal and are not modeled in the simulation.

- It is assumed that the criteria selected using the one channel model will be applicable to the geometry of the two channel model.

### *1.4.3  Seven Channel Model*

- It is assumed that the entry region prior to channel separation is sufficient in length to produce a fully developed flow suitable for an accurate representation of operational flow.

- Due to the high velocity and pressure within the channel the effects on the flow resulting from gravity are minimal and are not modeled in the simulation.

- The actual experiment will include instruments within each channel. It is assumed that this instrumentation will not have a significant effect on the fluid flow and thus are not modeled in the simulation.

- The geometry of the model is assumed to be perfect. In reality this will not be the case as there will be minor imperfections that may lead to slightly different results.

- It is assumed that the criteria selected using the one channel model and checked in the two channel model will be applicable to the geometry of the seven channel model.

## 1.5 Limitations

It is difficult to conduct a completely flawless study. Therefore in every study it is important to describe the known limitations.

### 1.5.1 One Channel

- This is a very basic representation of GTPA geometry. It does not include the two mixing regions or the two support combs. This will lead to a solution that is not an exact representation of what will happen within the GTPA.

- CFD is only an approximation of actual flow. Star-CCM+ makes many assumptions in order to make flow modeling easier. These assumptions could lead to a solution that is not an exact representation of actual flow which is why this is only an approximation.

- The simulation does not take into account any changes that would take place as a result of plate deflection. Many parameters within the model would change as a result of plate deflection but that is not modeled here.

- There is much data generated using CFD. It is not reasonable to analyze all of the data. Therefore, data will only be analyzed at certain points in each model in an attempt to get an idea of what is happening in the entire model.

### 1.5.2 Two Channel

- This model analyzes the larger center channel and one of the smaller side channels leading to an asymmetric geometry. The asymmetry of this model may cause it to respond differently than the full seven channel model.

- CFD is only an approximation of actual flow. Star-CCM+ makes many assumptions in order to make flow modeling easier. These assumptions could

lead to a solution that is not an exact representation of actual flow which is why this is only an approximation.

- The simulation does not take into account any changes that would take place as a result of plate deflection. Many parameters within the model would change as a result of plate deflection but that is not modeled here.

- There is much data generated using CFD. It is not reasonable to analyze all of the data. Therefore, data will only be analyzed at certain points in each model in an attempt to get an idea of what is happening in the entire model.

### 1.5.3  Seven Channel Model

- CFD is only an approximation of actual flow. Star-CCM+ makes many assumptions in order to make flow modeling easier. These assumptions could lead to a solution that is not an exact representation of actual flow which is why this is only an approximation.

- When determining the potential of plate deflection, the fact that the materials used in the HMFTF are not the exact same materials used in the HPRR's could cause different results.

- The simulation does not take into account any changes that would take place as a result of plate deflection. Many parameters within the model would change as a result of plate deflection but that is not modeled here.

- There is much data generated using CFD. It is not reasonable to analyze all of the data. Therefore, data will only be analyzed at certain points in each model in an attempt to get an idea of what is happening in the entire model.

## 2  SURVEY OF LITERATURE

This is not the first study conducted on plate deflection of nuclear fuel assemblies. It is also not the first time CFD has been used for these types of analyses. This chapter includes a summary of some pertinent articles that are relevant to this study.

### 2.1  Plate Deflection

The study of the deflection of plate-type fuel has taken place for many years. These studies are important in order to improve the efficiency of plate-type nuclear reactors. One of the earliest major studies conducted in this area was performed by Daniel R. Miller [5]. Miller's analysis gives a basic idea of how the plates within a plate-type fuel assembly tend to deflect. The plates will deflect symmetrically and in an array of fuel plates they will alternate with some deflecting towards each other while the next plates will deflect away from each other. This is shown in Figure 2.1.
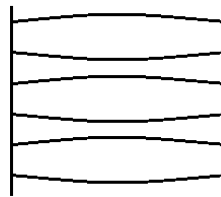


Figure 2.1: Example of plate deflection

This image shows an assembly containing six fuel plates, which are represented by the dark lines, and shows only five full flow channels. There are three flow channels where the plates are deflected away from each other and two, which are bordered by the three, where the plates deflected towards each other.

Miller used the equation for the pressure required to cause a flat wide beam to buckle in conjunction with Bernoulli's theorem for incompressible flow in order to determine the velocity required to produce forces of such magnitude to cause the fuel plate to buckle. Miller called this velocity the critical velocity. Miller developed an equation

for critical velocity for five different cases. These cases included both flat plate and curved plate geometries each with different edge supports. The first case analyzed in Miller's study was for a flat plate with built-in, or clamped, boundary conditions. The other two edges are considered to be free making the boundary conditions for this case F-C-F-C. The equation, according to wide beam theory, for the pressure required to deflect a plate under these conditions is shown.

$$y = \frac{px^2\left(1-v^2\right)\left(x^2 - 2bx + b^2\right)}{24EI} \tag{2.1}$$

Where $y$ is the deflection of the plate relative to the edge supports, $p$ is the pressure difference required to cause the plate to bend, $x$ is the longitudinal distance from the edge support, $b$ is the width of the plate, $v$ is Poisson's ratio of the plate material, $E$ is Young's Modulus of the plate material, and $I$ is the moment of inertia per unit width of the beam.

The plate on the other side of the channel will deflect symmetrically according to the same equation. Therefore, to obtain the total change in cross sectional area this equation is integrated with respect to $x$ from 0 to $b$ and multiplied by 2. To obtain the total change in cross sectional area per unit area this equation is divided by $bh$. After performing these calculations and substituting for the area moment of inertia $a^3/12$ the following equation is the result.

$$\frac{\Delta S}{S} = \frac{\left(1-v^2\right)pb^4}{30Ea^3h} \tag{2.2}$$

Where $S$ is the original, undeflected, cross-sectional area, $\Delta S$ is the total change in cross sectional area, $a$ is the thickness of the plate, and $h$ is initial flow channel height at the midspan of the channel.

The pressure differential developed across the plate is derived from Bernoulli's theorem and can be simplified assuming that the plate undergoes very small deformation.

$$p = \frac{2\rho V_0^2 \Delta S}{gS} \tag{2.3}$$

Where $\rho$ is the density of the coolant, $g$ is the acceleration due to gravity, and $V_0$ is the linear velocity of the coolant.

By substituting Equation (2.2) into Equation (2.3) determines the critical velocity for the given conditions.

$$V_{cr} = \sqrt{\frac{15gEha^3}{\rho b^4 (1-v^2)}} \tag{2.4}$$

Where $V_{cr}$ is the velocity required to cause a plate to buckle.

Although most of the analysis conducted by Miller was done on an assembly containing an array of plates, he also looked at how the critical velocity would change if he analyzed just a single plate. He found that the critical velocity approximation for a single plate was higher by a factor of $\sqrt{2}$. Miller mentions a few experiments that provide data that lend support to his formulas but also mentions that it would be beneficial to conduct experiments to determine the validity of his approximations [5].

Miller's desire for supporting experimental data was later fulfilled as other researchers conducted experiments with the purpose of providing experimental data to verify Miller's approximations. Smissaert found that plates begin to experience static deflection at low velocities and that the plates experience dynamic deflection at about

two times Miller's velocity which he refers to as the 'flutter velocity' [6, 7]. These results indicate that Miller's equation is a reasonable approximation for when plates will begin to experience measurable deflection.

Another study conducted by Ho gives evidence that Miller's velocity may not be as conservative as Smissaert suggests. His experimental study examined an assembly containing two fuel plates and used light water at 25 °C. Ho found that the plates in this study collapsed at about 78% of Miller's approximation. One method implemented in this study for the determination of plate collapse was the measure of the pressure drop through the channels [8]. The pressure drop through a channel can differ as a result of different channel cross-sectional areas leading to different velocities.

Kane conducted an experiment where he studied an assembly containing an array of plates. In this study Kane manufactured deviations or imperfections at the inlet of the channels between the fuel plates. These deviations caused the pressure and velocity to change within the channels resulting in deflection. Kane noted that the velocity calculated using Miller's equation was the velocity at which significant deflections were initially observed. Kane also noticed that these slight deviations at the inlet of the channel had a significant effect on the deflection through the channel especially at velocities greater than Miller's approximation [9].

Later Kane partnered with Groninger to conduct another experimental study of plate deflection. The results of this study were that plate deflection occurred at very low velocities. One major observation is somewhat related to Kane's previous work in that the critical velocity deflection is essentially a magnification of a pre-existing imperfection in the fuel plates. Here as with other studies, plates were observed to deflect in opposite directions as was observed by Miller and is shown in Figure 2.1. It

is mentioned that this only occurred at high flow rates and that at low flow rates this is not necessarily the case [10].

Oak Ridge National Laboratory (ORNL) examined fuel plates representing the Advanced Test Reactor (ATR) geometry. The study is very similar to the one presented in this work however, it was experimental and this study is computational. During the ORNL study the fuel plates were subjected to a series of tests at varying temperatures and flow rates. The pressure drop through each channel in the fuel assembly was measured in conjunction with channel deflections. The results of this study lead to the inclusion of venting holes spaced periodically in the side plates to help distribute the flow more evenly causing the pressure differences between the channels to be less severe making plate deflection less likely [11].

Rosenberg and Youngdahl used similar assumptions for flat plates supported uniformly along the axial edges and came up with similar results. The paper mentions that at sufficiently high velocities the plates diverge but at lower velocities the plate motion is not clearly affected by the presence of the fluid [12].

Johansson considered the effect of frictional pressure drop through the channel as well as the flow redistribution between constricted and expanded channels. These effects had not been taken into account in other studies up to this point. Johansson noted that the frictional pressure drop is larger through a constricted channel than it is through an expanded channel. He noted that these effects cause the deflected region to move downstream as the plate continues to deform [13].

Davis and Kim found through numerical analysis that flat plates are expected to begin to deflect at velocities that are about 1.1 times Miller's approximated critical velocity for both clamped and simply supported edges. The results show that the plates would experience minor deflections and not a sudden collapse as Miller expected. Davis and

Kim also found that the plates would begin to vibrate, or experience dynamic divergence, at about two times Miller's approximation [14, 15].

Guo et al. did analyses on single plates as well as multiple plates similar to Miller's study. They found that a single plate gives a more conservative approximation for static critical velocity than an array of plates. They also concluded that using a single plate to predict dynamic instability was an unsafe approach and instead recommended using an array of plates for this analysis [16].

Smith focused his studies on flat plates and used a few different assumptions than Miller did. Using these assumptions he developed a similar equation for critical velocity to Miller's. The resulting equation is shown below.

$$V_{cr} = \sqrt{\frac{15 g E h a^3}{\rho b^4 \left(1 - v^2\right)}} \cdot \sqrt{\frac{1}{\frac{1}{2}\left(1 + \frac{4\pi v l h}{b^2}\right)\left(1 + \frac{4 v l^2}{3 b^2}\right)}} \tag{2.5}$$

The equation is only a variation of Miller's approximation. The end result is still dependant on all of the same parameters with the addition of effective plate length $l$ [17]. The work of Miller, Smith, and other scientists shows that the material used for the fuel plate, the coolant, and the geometry of the plate and channel are a few of the parameters of plate deflection.

## 2.2 Solid Mechanics

Since the geometry of the channel is one of the primary contributing factors to plate deflection it is important to analyze some of the contributing factors to changes in this geometry. If the cross-sectional area between these channels is different this could in turn lead to plate deflection. It is important to take note of the factors present in a nuclear reactor that could contribute to this difference in channel cross sectional area.

A likely contributing factor to inconsistent flow channel spacing results from geometric tolerance stack-up. The fuel plates and their adjacent channels are relatively narrow (~0.05 in), considering the absolute tolerances of this geometry to be of the order ±0.01 inches has potential to result in a percent tolerance up to ±20% of a given flow channel. Another contributing factor to geometric differences occurs as a result of the operation of the reactor. The ATR SAR lists a few of these [3].

- Build-up of oxidation product on the surface of the fuel plate due to a chemical interaction between the 6061-0 aluminum and the cooling water.
- Growth and swelling of fuel plates affects the thickness of the plate.
- Blistering occurs when there is an excessive build-up of fission gases either at the fuel-cladding interface or within the fuel core.
- Fuel element bowing through thermal expansion caused by temperature differentials.

Each of these could potentially lead to a difference in cross sectional area between the channels. The ATR SAR states that with proper controls none of these cause significant problems within the ATR [3]. However, with a different fuel type and geometry these could prove to be more of a problem which is another reason why the tests conducted in the HMFTF are important.

The material properties of the plate are also a contributing factor to plate deflection. With this being the case it is important to understand why aluminum was selected for the cladding since it is not as strong as other options for plate cladding and also has a relatively low melting temperature. The ATR SAR provides the reason for the selection of the aluminum cladding [3]. Aluminum is used because it has a low absorption cross-section leading to a high neutron flux which is one desired capability of the USHPRR's. The aluminum alloy 6061 has a sufficient strength to withstand the normal operational conditions of the reactor, but is also light and easy to work with. The thermal conductivity is high and provides efficient heat transfer. These

advantages outweigh the disadvantages associated with this fuel which justify its selection as a cladding material [3].

## 2.3 Support Combs

Although the plates tend to deflect along the entire plate length, many studies have indicated that the leading edge of the fuel plate is the most susceptible to plate deflection due to it not being supported and thus, being less stiff then the other portions of the plate. Occasionally in an attempt to stiffen the leading edge of the plate a support comb is installed. A support comb is installed in such a way that the plates are supported between the "teeth" of the comb. Since the primary focus of the analysis of the GTPA is the fuel foil, and since the first quarter inch of the plate is only cladding[18], it is essential that deflection occur further downstream of the leading edge. In order to make sure that this happens a support comb, shown in Figure 1.3, will be used.

The study performed by Kane also states that deflection is more likely to occur at an unsupported leading edge and that in order to prevent this from happening a support comb should be used. [9]. Kane's other study conducted primarily by Groninger concludes that the support comb does indeed stiffen the leading edge and that significant deflections still occur two or three spans downstream of the leading edge for the geometry studied in his analysis. Their study also indicated that channels with a larger height benefit more from the support combs [10]. Smisseart also noticed that small channels seem to be less affected by the presence of a support comb. He noted that channels with heights that are smaller than one sixteenth of an inch are still affected by the Bernoulli forces on the plate and do not benefit from the support comb [6, 7]. This is not an issue for the current study because the smallest channel height is 0.075 inches which is larger than one sixteenth of an inch, which is equal to 0.0625 inches.

Johansson also considered support combs in his study. He observed that the critical velocity at the inlet of the fuel plate is lower than further downstream indicating that it is not as stiff and thus, more susceptible to plate deflection. He observed that the instillation of a support comb significantly increased the local stiffness at the leading edge which increased the critical velocity in that area by a factor of three or four. Johansson also observed, as did Groninger and Kane that with the instillation of a support comb the deflections still took place about two span widths downstream of the inlet [13].

## 2.4   CFD Analysis

One method that is often implemented to analyze flow through a fuel assembly is Computational Fluid Dynamics (CFD). CFD is used to simulate fluid flow and heat transfer for different scenarios. CFD is very versatile and can be applied to many different situations and numerous industries. CFD can be a very useful tool but unless some basic procedures are followed it could generate a misleading and incorrect solution.

Yoo used CFD to study the flow of air through a dry cask storage system. In his study he provided a procedure to follow when performing CFD studies [19]. The first step in any CFD analysis is to clearly define the geometry that is to be analyzed. Once an appropriate geometry is created a grid size must be selected. The grid size is selected after performing a grid sensitivity study [19]. There are two parameters to take note of when conducting a grid sensitivity study. These are computation time and accuracy. As the grid becomes finer the solution tends to become more accurate. However, with more cells in the grid the computation time required to achieve a solution also increases. Therefore, the purpose of a grid sensitivity study is to achieve a reasonable balance between these two parameters. The grid must be refined enough to achieve a reasonably accurate solution without taking an excessive amount of time to come to that solution.

Yoo's sensitivity study monitored the peak cladding temperature of the fuel assembly as the parameter to follow to determine if a grid independent solution had been achieved. A grid independent solution does not change for at least two grid refinements [19]. A similar procedure was followed to select an appropriate discretization scheme and precision. The last parameter of importance according to Yoo's paper was the selection of appropriate boundary conditions [19]. This same practice is implemented by others in their CFD analysis [20-24].

It is very important in a grid sensitivity study to ensure that an appropriate grid size is selected. If the grid size is too coarse then an incorrect solution may be generated. If a grid size is too fine then it may take an excessive amount of time to converge on a correct solution. In some cases an over-refined grid can lead to an incorrect solution due to the cumulative numerical round-off error as was mentioned by Tan et al. in his analysis [25, 26].

Ha and Garland conducted an experimental study and compared the results with those generated using a CFD simulation. The study consisted of measuring the pressure drop through a fuel assembly with a plate-type design. They used the results of the experimental studies to verify the results that they obtained in the CFD simulations in an attempt to justify the use of the CFD in safety analysis for the McMaster nuclear reactor. The results of the study indicated that they could use a 2D CFD code to analyze the flow in the channels of the fuel assembly. They also found that they could use a simple 1D correlation to estimate the pressure drop in various assemblies in the core [27].

One study that was validated with experimental results was that conducted by Srivastava et al. This study analyzed a single rectangular flow channel. The results indicated that the CFD simulation was a good representation of the experimental results indicating that CFD is a good method for modeling this type of flow [28]. It is

very important to validate CFD codes with experimental data otherwise it is unclear if the code generates an accurate solution. Many CFD studies have done this experimental validation [29-32].

Calis et al. performed a study using CFD to study the pressure drop through packed pebble bed reactors. Although it does not directly relate to the current study there are a few important comparisons. Not only did Calis et al. follow standard CFD practices, but they also compared the results of two turbulence models. They compared the results generated using the Reynolds Stress Model (RSM) with the results generated by the k-ε model. Their conclusion was that the k-ε model would be sufficient to use because the results were within 10% of the RSM for their particular study [33].

# 3   MODELS AND METHODS

This chapter outlines the methods used to model the one, two, and seven channel geometries. The information used for each CFD simulation is presented as well as any information needed for post-processing analysis.

All numerical results presented herein were acquired through the use of Star-CCM+ version 5.04.008. Star-CCM+ is a CFD tool which enables the user to specify boundary conditions and initial conditions for a prescribed geometry within its solution domain. This enables the tool to explicitly solve for the flow and pressure in that domain. All *cases* that were considered as part of this study are outlined in this chapter. A *case* refers to a specific geometry, mesh type, mesh refinement, turbulence model, and initial and boundary conditions. If any one of those parameters is changed a new *case* is created.

## 3.1   One Channel Model

The one channel model is used to make the selection of mesh type, turbulence model approach, and mesh size. It is a simple geometry that does not include the two mixing regions or the two support combs.

### 3.1.1  File Organization

A unique filename was given to each *case* producing a total of 12 input files for the one channel model analysis. Each filename is assigned a model number. The filenames with their associated model numbers are given in Table 3.1. For the remainder of the document the filenames will be referenced by the model number.

Table 3.1: One channel model filenames and model numbers

| Model # | Filename |
|---------|----------|
| 1.1 | 0.5 tetra mesh k-e.sim |
| 1.2 | 0.5 tetra mesh RSM.sim |
| 1.3 | 0.25 tetra mesh k-e.sim |
| 1.4 | 0.21 tetra mesh k-e.sim |
| 1.5 | 0.5 poly mesh k-e.sim |
| 1.6 | 0.5 poly mesh RSM.sim |
| 1.7 | 0.25 poly mesh k-e.sim |
| 1.8 | 0.25 poly mesh RSM.sim |
| 1.9 | 0.1 poly mesh k-e.sim |
| 1.10 | 0.1 poly mesh RSM.sim |
| 1.11 | 0.01 poly mesh RSM.sim |
| 1.12 | 0.0075 poly mesh RSM.sim |

## *3.1.2  Geometry*

As outlined by Yoo, the first step in creating a CFD model is to create the geometry that will be analyzed. The channel that will be analyzed in the one channel model is a channel with a height of 0.075 inches. This geometry does not include the support combs or entry regions. The channel width is 3.5 inches and the length of the channel is 24 inches as shown in Figure 3.1.
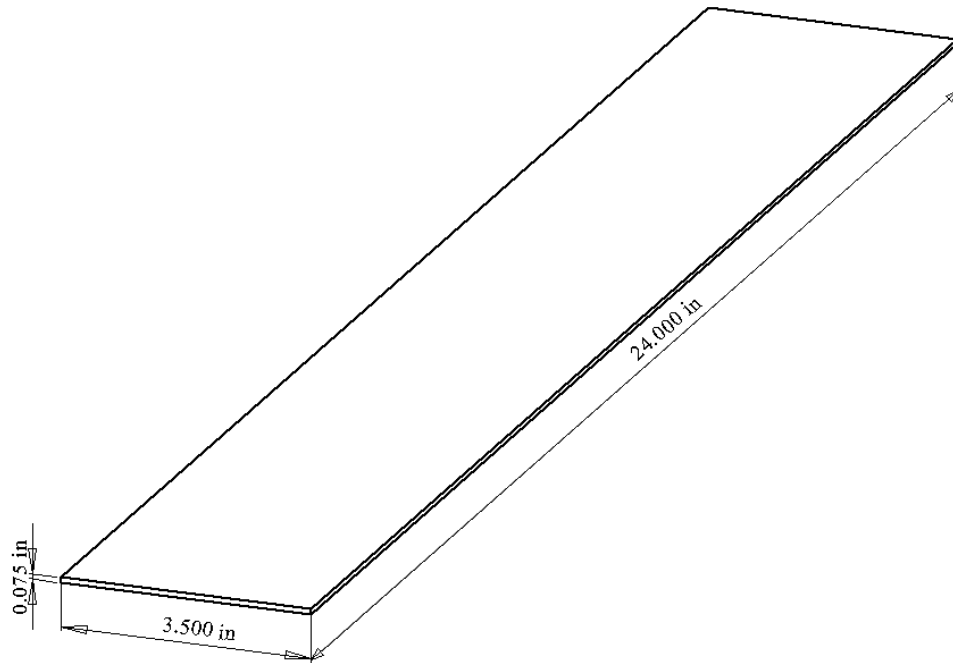
Figure 3.1: One channel model dimensions

### 3.1.3 Mesh Size

With a completed geometry, Yoo indicated that the next step is to generate a mesh for the given geometry. The mesh is made up of small cells or prisms. Each of these cells make up individual calculation regions where the flow is calculated and simulated. If there are a small number of cells the mesh is considered coarse and the solution will not have many data points. If there is a large number of cells the mesh is fine and has many data points and is likely more accurate than a coarse mesh. It is important that the mesh be refined appropriately in order to develop an accurate solution. There are many components of a CFD mesh. The mesh type, which will be discussed later, affects the shape of the cells in the mesh. The Surface Remesher is a basic feature that helps to improve the quality of the surface mesh and works well with the prism layer mesher to ensure that all the cells blend well with one another. The Prism Layer meshing model was also implemented in this study. This model enables the mesh at the edge of the geometry to be more refined than the mesh in the center of the

geometry. This is done because there is a larger velocity gradient at the wall. To specify the prism layer mesh, the user enters information about the number of cells desired in the prism layer, the growth rate from one cell to the next, and the total thickness of the prism layer. The total thickness can either be entered as an absolute value or as a percentage of base size. Base size contributes not only to the prism layer thickness but also to other mesh parameters such as surface size and potentially prism layer thickness. Surface size can also be entered as an absolute value or as a percentage of base size. Surface size determines the size of the cells next to the surface. These surface cells are used with the surface remesher to generate the rest of the cells throughout the entire geometry. This study includes six different refinement levels. The details of each level of refinement are shown in Table 3.2.

Table 3.2 : Refinment levels

| Refinement Level | Base Size (m) | Surface Size (% of Base) | # of Prism Layers | Prism Layer Stretching | Absolute Prism Layer Size (m) |
|---|---|---|---|---|---|
| 1 | 0.5 | 25 | 5 | 1.1 | $3.33 \times 10^{-4}$ |
| 2 | 0.25 | 25 | 5 | 1.1 | $3.33 \times 10^{-4}$ |
| 3 | 0.21 | 25 | 5 | 1.1 | $3.33 \times 10^{-4}$ |
| 4 | 0.1 | 25 | 5 | 1.1 | $3.33 \times 10^{-4}$ |
| 5 | 0.01 | 25 | 5 | 1.1 | $3.33 \times 10^{-4}$ |
| 6 | 0.0075 | 25 | 5 | 1.1 | $3.33 \times 10^{-4}$ |

For the one channel model the number of cells that each of these refinement levels represent are given in Table 3.3.

Table 3.3: One channel model cell count as governed by level of refinement

| Refinement Level | # of Cells |
|---|---|
| 1 | 3779 |
| 2 | 11455 |
| 3 | 36440 |
| 4 | 54087 |
| 5 | 1005896 |
| 6 | 1040875 |

## 3.1.4 Mesh Type

The two mesh types that were analyzed were the polyhedral mesh type and the tetrahedral mesh type. The axial pressure drop relative to the inlet was compared for both mesh types. The mesh type was the only differing variable in each comparison. The models that were compared directly are shown in Table 3.4 with the models that share a row being those that were compared.

Table 3.4: Tetrahedral and polyhedral model comparisons of pressure drop

| (Tetra) Model # | (Poly) Model # |
|---|---|
| 1.1 | 1.5 |
| 1.2 | 1.6 |
| 1.3 | 1.7 |

To collect pressure drop data from these models as well as from future models, nine line probes were drawn axially from the inlet of the channel to the outlet with about 100 data points per line probe. These nine line probes were positioned in such a way that there were three across the top, three across the middle, and three across the bottom of the channel as shown in Figure 3.2. These nine probes were later used in both the two channel and the seven channel model which is why the vertical dimension includes two lengths.
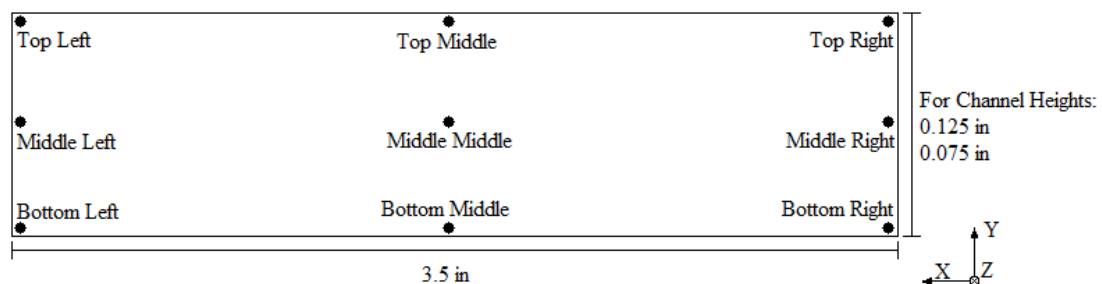


Figure 3.2: Line probes in the x-y plane

The pressure values from these line probes were initially compared using a T-test and these comparisons were used to make the selections for mesh type, turbulence model,

and mesh size. However, after further analysis, the T-test proved not to be applicable for these data sets. Therefore, the selections were checked by comparing the data using an average percent difference comparison given later in Equation (3.1). The results from these comparisons are discussed in detail in Section 4.1.1.

### 3.1.5  Continua and Physics Models

There are four different methods for turbulence modeling. These are the Reynolds Averaged Navier-Stokes (RANS), Large Eddy Simulation (LES), Detached Eddy Simulation (DES), and Direct Numerical Simulation (DNS) [34].

The RANS equations focus on mean flow and effects of turbulence on mean flow properties. The RANS equations use time or ensemble averaged Navier-Stokes equations. The time averaged flow equations have extra terms due to the interactions between turbulent fluctuations. The most common way of modeling these equations is with the k-ε and RSM approaches [34].

The LES method is an inherently transient technique that tracks the portion of the larger eddies by space filtering the unsteady Navier-Stokes equations prior to computation of each iteration. Although this approach gives a good model of turbulent flow it is also computationally expensive [34].

The DES is a modeling approach that uses features from both the RANS and LES approaches. The LES is used for the unsteady and separated scales of the flow where the RANS is used for the shear layers [34].

The DNS does not use any turbulence model but instead, as the name suggests, simulates turbulent flow directly. Although this method is very accurate it is also very costly with regard to computer resources. It is also best to use on simple geometries because complex geometries are, in general, too large to reasonably solve [34].

This analysis is conducted under steady-state conditions therefore the transient capabilities of the LES and DES are not required, or able to be used. Therefore, the RANS model was selected. There are four different available approaches in Star-CCM+ to use to solve the RANS based transport equations. These are k-ε, k-ω, RSM, and Spalart Allmaras. The Spalart Allmaras and the k-ω models are similar in design and don't work as well for free-shear layer flows [34]. Therefore, they were not considered in this analysis. The RSM is known to be a better approach for high Reynolds numbers than the other options and would be the best approach to use [35]. However, it is very computationally expensive when compared with other approaches. The k-ε has been described as having a good balance between robustness, computational cost, and accuracy [34]. Therefore, the k-ε model was analyzed to determine if it would be an appropriate alternative to the RSM. If the results generated by the two approaches are similar, then the k-ε model can be used. A delineation of all models and their corresponding mesh types and reference values are given in Table 3.5.

Table 3.5: Mesh type and mesh reference values

| Model # | Mesh Type | Refinement Level | Turbulence Model |
|---------|-----------|------------------|------------------|
| 1.1 | Tetrahedral | 1 | k-ε |
| 1.2 | Tetrahedral | 1 | RSM |
| 1.3 | Tetrahedral | 2 | k-ε |
| 1.4 | Tetrahedral | 3 | k-ε |
| 1.5 | Polyhedral | 1 | k-ε |
| 1.6 | Polyhedral | 1 | RSM |
| 1.7 | Polyhedral | 2 | k-ε |
| 1.8 | Polyhedral | 2 | RSM |
| 1.9 | Polyhedral | 4 | k-ε |
| 1.10 | Polyhedral | 4 | RSM |
| 1.11 | Polyhedral | 5 | RSM |
| 1.12 | Polyhedral | 6 | RSM |

Data for the mesh type comparative analysis was collected using the nine line probes from Figure 3.2. The models that were compared in this analysis are shown in Table 3.6 with the models that share a row being those that were compared.

Table 3.6: RSM and k-ε model comparisons of pressure drop

| (k-ε) Model # | (RSM) Model # |
|---|---|
| 1.5 | 1.6 |
| 1.7 | 1.8 |
| 1.9 | 1.10 |

Table 3.7 shows the inputs for each physics model.

Table 3.7: Differences between k-ε and RSM inputs

| k-ε Turbulence Models | Reynolds Stress Turbulence Models |
|---|---|
| Three Dimensional | Three Dimensional |
| Steady | Steady |
| Liquid (H20) | Liquid (H20) |
| Coupled Flow | Coupled Flow |
| IAPWS-IF97 (Water) | IAPWS-IF97 (Water) |
| Coupled Energy | Coupled Energy |
| Turbulent | Turbulent |
| Reynolds-Averaged Navier-Stokes | Reynolds-Averaged Navier-Stokes |
| K-Epsilon Turbulence | Reynolds Stress Turbulence |
| Realizable K-Epsilon 2-Layer | Linear Pressure Strain Two-Layer |
| Two-Layer All y+ Wall Treatment | Two-Layer All y+ Wall Treatment |

The first selection was chosen by default. The geometry being analyzed is three dimensional so the physics model used to analyze that geometry also needs to be three dimensional.

The testing done in the HMFTF will be under steady state conditions. Therefore, steady was selected instead of implicit unsteady. This is the same reason IAPWS-IF97 (Water) was chosen for the fluid. The other choices were constant density, polynomial density, and user defined density. These other options are not as suitable as water because with water selected the simulation can calculate the density accordingly with

the changes in pressure and temperature. With the selection of water, the software suggested using the coupled energy model. This model, in conjunction with the coupled flow model, solves equations for mass, momentum, and energy simultaneously. Segregated flow could have also been chosen, however, this would have led to longer computation time, especially with finer meshes, because the segregated flow model solves equations sequentially instead of simultaneously [34]. The flow through the assembly will be turbulent flow so the turbulent model was selected in order to represent the actual flow.

The two-layer wall treatment was chosen for both k-ε and for the RSM. A two-layer wall treatment divides the viscous sublayer into two layers in order to better calculate what is happening near the wall. Using this method, the values near the wall can blend smoothly with the values in the center of the channel. For this reason two-layer wall treatment was used for both approaches. For the k-ε model, there were two options for the two-layer wall treatment. These were the standard k-ε wall treatment and the realizable k-ε wall treatment. The Star-CCM+ user's guide indicates that the realizable wall treatment will generate results that are at least as accurate as the standard wall treatment but in many applications will generate a result that is more accurate than the standard wall treatment. Therefore the realizable wall treatment was used for the k-ε approach. For both the k-ε selection and the RSM selection a recommended subsequent selection is 'Two-Layer All y+ Wall Treatment.' y+ is a non-dimensional wall distance for wall bounded flow. The 'Two-Layer All y+ Wall Treatment' analyzes the flow for both low y+ values and high y+ values making it able to be used in many situations [34].

### 3.1.6  Initial Conditions

The initial conditions used in each model are given in Table 3.8. For the first few models initial conditions were set at the default values. When the meshes became finer, the computation time required for the simulation to converge became much longer. The initial conditions were adjusted to reduce compilation time.

Table 3.8: Initial conditions for one channel models

| Model # | Pressure (psig) | Temperature (F) | Turbulent Velocity Scale (m/s) | Velocity [x,y,z] (m/s) |
|---|---|---|---|---|
| 1.1 | 0.0 | 400 | 1 | [0.0, 0.0, 0.0] |
| 1.2 | 0.0 | 400 | 1 | [0.0, 0.0, 0.0] |
| 1.3 | 0.0 | 400 | 1 | [0.0, 0.0, 0.0] |
| 1.4 | 0.0 | 400 | 1 | [0.0, 0.0, 0.0] |
| 1.5 | 0.0 | 400 | 1 | [0.0, 0.0, 0.0] |
| 1.6 | 0.0 | 400 | 1 | [0.0, 0.0, 0.0] |
| 1.7 | 0.0 | 400 | 1 | [0.0, 0.0, 0.0] |
| 1.8 | 0.0 | 400 | 1 | [0.0, 0.0, 0.0] |
| 1.9 | 0.0 | 400 | 1 | [0.0, 0.0, 0.0] |
| 1.10 | 0.0 | 400 | 1 | [0.0, 0.0, 0.0] |
| 1.11 | 0.0 | 400 | 1 | [0.0, 0.0, 0.0] |
| 1.12 | 600.0 | 400 | 14 | [0.0, 0.0, 14.0] |

The under-relaxation factor (URF) for most of the simulations was set at the default value of 0.6. The value 0.6 is the highest recommended number for use with the RSM. If the value is set higher there is an increased possibility that the solution will not converge properly. The URF redefines the value for a given variable for the next iteration. A smaller URF will mean a smaller change in the value from one iteration to the next. With large changes, the solution may begin to diverge before it processes enough iterations to fix the divergent behavior. With a small URF the divergent behavior is less likely to get out of control. Using a smaller URF also leads to a longer time to converge so the value is only changed if absolutely necessary. The refined mesh used in Model 1.12 did not converge properly while implementing the 0.6 URF. Therefore the value was adjusted to 0.25 in order to ensure that the solution would converge. After the solution had been through enough iterations to fix any divergent behavior the URF was changed back to 0.6. This was done in an attempt to reach convergence faster.

## 3.1.7 Boundary Conditions

Table 3.9 shows the values that were used for the three basic boundary conditions in the one channel model. The velocity was 14 m/s which was used to calculate the inlet mass flow rate. The outlet was set as a pressure outlet and required a pressure input. The model is isothermal meaning that the temperature is the same for the inlet and the outlet.

Table 3.9: Boundary conditions for one channel models

| Boundary Condition | Inlet | Outlet |
|---|---|---|
| Inlet Mass Flow Rate (kg/s) | 2.042 | - |
| Outlet Pressure (psig) | - | 464.7 |
| Fluid Temperature (F) | 400.0 | 400.0 |

## 3.1.8 Grid Refinement

Using all outlined parameters a grid sensitivity study was conducted in order to achieve a grid independent solution. A grid independent solution is a solution that has one or more parameters that does not change significantly for two or more consecutively smaller grid sizes [19]. To determine what mesh size would be appropriate for the grid independent solution the refinement level became progressively finer and data from each refinement was compared. The models that were compared were Models 1.6, 1.8, 1.10, 1.11, and 1.12. After each refinement level the nine line probes from Figure 3.2 were used to collect pressure data that was used to determine if a grid independent solution had been achieved.

The T-test was also used for the initial comparisons and selection of a grid independent solution. The selection was later checked with an average percent difference method in conjunction with the uncertainty calculated using Richardson's Extrapolation.

The percent difference between the data sets was calculated using the percent difference equation.

$$\% \text{ Difference} = \frac{\text{Approximate Value - Exact Value}}{\text{Exact Value}} \times 100\% \tag{3.1}$$

Since this equation was used on two sets of approximated values the "Exact Value" from the equation was replaced with the value that was expected to be better from the two data sets. For the mesh type analysis this was the value from the polyhedral mesh type, for the turbulence model approach analysis was the value generated using the RSM approach, and for the grid sensitivity study this was the value from the finer mesh size. For each data set this value was calculated for every point along each line probe. An average of the values along each probe was calculated and this average percent difference value was the value reported in the results section.

Richardson's Extrapolation is used to determine the uncertainty associated with a CFD solution. Data from two grid sizes are needed to perform this analysis. The ratio of the number of cells between the two grids is used along with the order used in generating the solution. The equation for the uncertainty value was developed by Richardson[36] and given by Ferziger[37] to be:

$$\varepsilon = \frac{\varphi_1 - \varphi_2}{r^z - 1} \tag{3.2}$$

Where $\varepsilon$ is the value of the uncertainty, $\varphi_1$ is the value from the finer mesh, $\varphi_2$ is the value from the coarser mesh, $r$ is the ratio of the cells between the two meshes, $z$ is the order used in generating the solution. This value is then added to the value for the finer mesh to obtain the extrapolated value.

$$\Phi = \varphi_1 + \varepsilon \tag{3.3}$$

The only new variable here is $\Phi$ which represents the value obtained using Richardson's Extrapolation [37].

This value was obtained for the data of the two finest acceptable refinement levels, refinement level (RL) 4 and RL 6, for each line probe. This generated an extrapolated value for each point on each line probe. The percent difference between these extrapolated values and the pressure values of RL 6 was calculated. These percent differences were normalized using an L2 norm. The percent differences for the RL 4 and RL 6 were also normalized and the data was compared. If the value from the grid refinement study was less than the value from the uncertainty the solution is accurately classified as grid independent.

## 3.1.9  Summary

It is necessary to summarize the criteria that were selected using the one channel model as this is the input criteria that will be used for the two channel model. Chapter 4 discusses the results in detail and outlines why each of these selections were made. A summary of the selections are given in Table 3.10.

Table 3.10: Summary of selected criteria

| Parameter | Selection |
|---|---|
| Turbulence Model Approach | RSM |
| Mesh Type | Polyhedral |
| Mesh Refinement | Refinement Level 6 |
| Number of Prism Layers | 5 |
| Prism Layer Stretching | 1.1 |
| Prism Layer Thickness | $3.33 \times 10^{-4}$ m |
| Initial Turbulent Velocity Scale | 14 m/s |
| Velocity [x,y,z] | 14 m/s |
| Temperature | 400.0 °F |
| Pressure Outlet | 464.7 psig |
| Mass Flow Rate (kg/s) | 2.042 kg/s |

## 3.2 Two Channel Model

The two channel model includes the same 0.075 inch channel that was analyzed in the one channel model analysis as well as the 0.125 inch channel. The analysis of the two channel model is a preliminary check to ensure that the criteria selected in the one channel model analysis will produce similar results if the geometry is changed slightly and to determine if there are any obvious errors in the input data before moving on to the seven channel model.

### 3.2.1 Geometry

As with the one channel model the first step is to create the geometry that is to be analyzed. The geometry, with the dimensions, is shown in Figure 3.3.
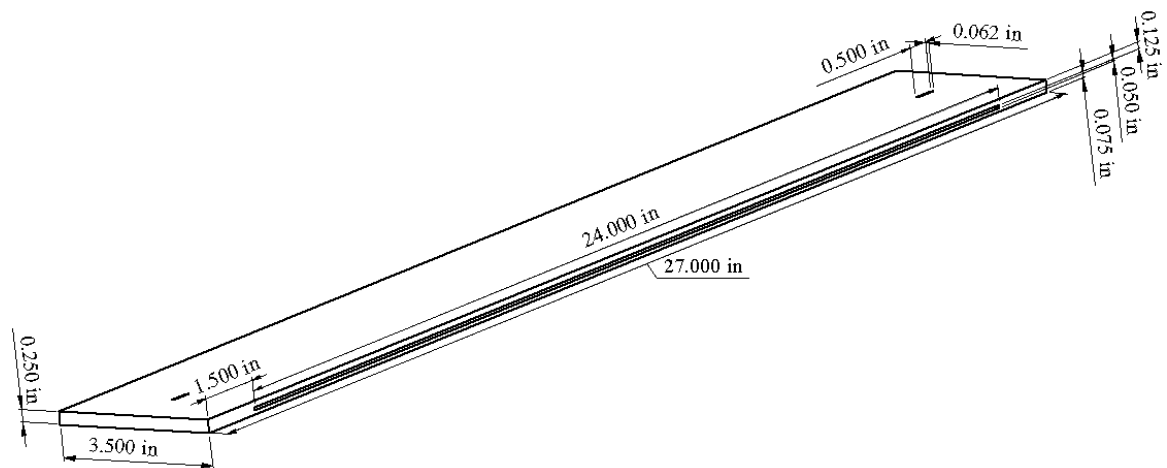


Figure 3.3: Dimensions of two channel model

This model included mixing regions at the inlet and the outlet that were each 1.5 inches long. The inlet and outlet support combs were also modeled in this geometry. Each support comb was 0.062 inches wide and 0.5 inches long and were located 1.25 inches from the inlet and outlet respectively. The total width of the model is 3.5 inches. The 0.075 inch channel had the same dimensions as the channel modeled in the one channel model simulation. The fuel plate in between the two channels was 0.05 inches. The addition of the 0.125 inch channel makes the total height of this

model is 0.25 inches. The total length, which is made up of the 24 inch channel and the two 1.5 inch mixing regions, is 27 inches.

## 3.2.2  Model Setup

The input criteria used in the one channel model were used again for this model. Therefore the velocity was 14 m/s. However with a different geometry this led to a calculated mass flow rate of 6.8 kg/s. Therefore, there was only one *case* analyzed in this study. The filename and model number of this *case* are given in Table 3.11.

Table 3.11 : Two channel model filename and model number

| Model # | Filename |
|---------|----------|
| 2.1 | 0.0075 poly mesh RSM 2 channel.sim |

Model 2.1 uses refinement level 6 and the associated number of cells is given in Table 3.12.

Table 3.12: Cell count of two channel model

| Model # | # of Cells |
|---------|-----------|
| 2.1 | 331557 |

The initial conditions for this model were the same as those used for Model 1.12. These are given in Table 3.13.

Table 3.13: Initial conditions for two channel model

| Model # | Pressure (psig) | Temperature (F) | Turbulent Velocity Scale (m/s) | Velocity [x,y,z] (m/s) |
|---------|-----------------|-----------------|--------------------------------|------------------------|
| 2.1 | 600.0 | 400 | 14 | [0.0, 0.0, 14.0] |

The boundary conditions for the pressure and the temperature for these models remained the same as those used in Model 1.12 and the mass flow rate changed in accordance with the description above. The resulting boundary conditions are shown in Table 3.14

Table 3.14: Boundary conditions for two channel model

| Boundary Condition | Inlet | Outlet |
|---|---|---|
| Model 2.1 Mass Flow Rate (kg/s) | 6.8 | - |
| Pressure (psig) | - | 464.7 |
| Fluid Temperature (F) | 400.0 | 400.0 |

Therefore the only selection that is different from Table 3.10 for Model 2.1 is the mass flow rate. The other selections are the same as for Model 1.12.

### 3.2.3 Analysis

The two channel model provides the first opportunity to observe pressure differences between channels. Due to the difference in cross-sectional area the pressure drop is expected to be different in each channel. It is expected that the pressure drop through the two channel model will follow the same trend as was observed in the one channel model but will also show some noticeable differences due to the difference in geometry. The nine line probes from Figure 3.2 were used in the 0.075 inch channel as well as in the 0.125 inch channel to collect data through these two channels.

The cross-sectional velocity in each of the two channels was analyzed using a series of five additional line probes for each channel. These line probes were located a quarter of the span-width, 0.875 inches, away from the edge of the channel. The five probes were placed along the length of the channel at locations relative to the inlet of the two channels of 0 inches, 6 inches, 12 inches, 18 inches, and 24 inches. A diagram showing the location of these probes is given in Figure 4.5.
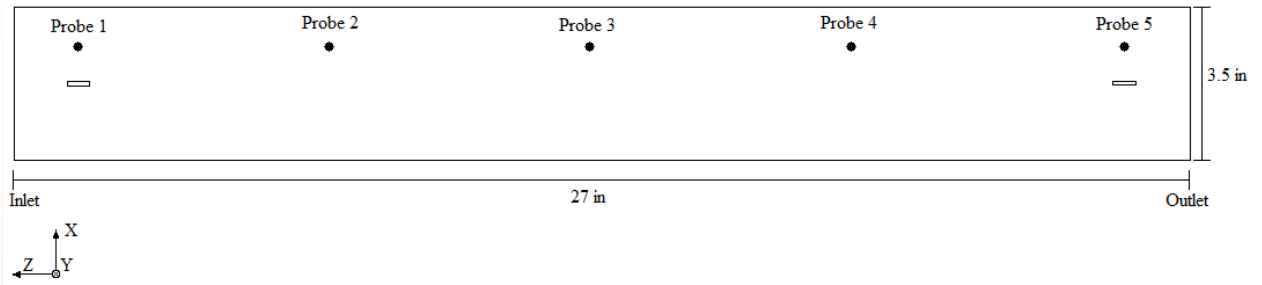
Figure 3.4: Velocity profile line probe locations

These line probes were used in the 0.125 inch channel as well as the 0.075 inch channel and the data from each channel was compared.

## 3.3   Seven Channel Model

This model includes the full array of plates and flow channels as well as the inlet and outlet mixing regions and both support combs. Five unique *cases* are analyzed for this model to determine the effect that these different boundary conditions have on plate deflection.

### 3.3.1  Geometry

The seven channel geometry was very similar to that of the two channel model geometry in that there were entry and exit mixing regions and support combs. The seven channel model added 5 more 0.075 inch channels each separated by a 0.05 inch fuel plate. This model with the associated dimensions is, shown in Figure 3.5.
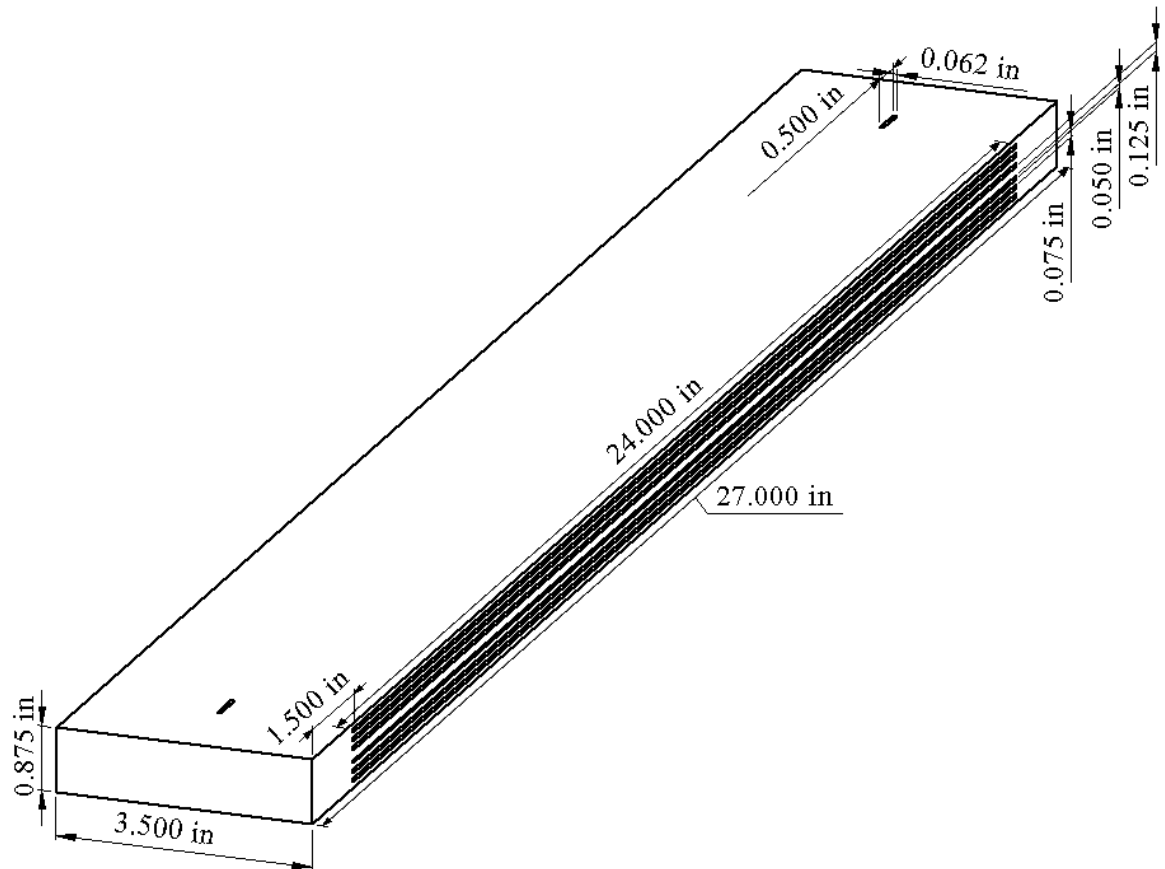
Figure 3.5: Dimensions of seven channel model

## 3.3.2 Model Setup

The seven channel model was analyzed using five different *cases* that were analyzed using slightly different criteria for the system temperature and flow rate. These *cases* are a portion of the *cases* that were used for the full test matrix analysis of the HMFTF and have the same associated *case* numbers as shown in Table 3.15. For the seven channel model *case* numbers were used instead of model numbers because each model already had an associated *case* number and it would be redundant and confusing to assign another number to each model.

Table 3.15: Seven channel model filenames and case numbers

| Case # | Filename |
|--------|----------|
| 1 | 7_Channel_Case_1.sim |
| 4 | 7_Channel_Case_4.sim |
| 7 | 7_Channel_Case_7.sim |
| 8 | 7_Channel_Case_8.sim |
| 9 | 7_Channel_Case_9.sim |

The cell count for each of these *cases* is the same. Each *case* uses RL 6 and the cell count for these models is given in Table 3.16.

Table 3.16: Cell count for seven channel models

| Case | # of Cells |
|------|-----------|
| All | 1044291 |

The only parameters that changed in the input criteria from the two channel model to the seven channel model are those that are shown in Table 3.17.

Table 3.17: Input parameters for the seven channel *cases*

| Case # | Temperature (°F) | Mass Flow Rate (kg/s) | Volumetric Flow Rate (gpm) | Outlet Pressure (psig) |
|--------|------------------|-----------------------|----------------------------|------------------------|
| 1 | 120 | 11.2 | 179 | 429.5 |
| 4 | 120 | 12.7 | 204 | 429.5 |
| 7 | 120 | 14.3 | 229 | 429.5 |
| 8 | 250 | 13.6 | 229 | 429.5 |
| 9 | 350 | 12.8 | 229 | 429.5 |

The first three *cases* have the same temperature but varying volumetric flow rate. The last two *cases* have the same volumetric flow rate as *Case* 7 but each have a different temperature. The reason the mass flow rates are different for *cases 7, 8,* and *9* is because the density of the water decreases with the increase in temperature. Therefore, since the equation to convert volumetric flow rate to mass flow rate is dependent on density, the mass flow rate is different. This is done according to Equation (3.4).

$$\dot{m} = \rho \cdot Q \tag{3.4}$$

Where $\dot{m}$ is the mass flow rate, $\rho$ is the density, and $Q$ is the volumetric flow rate.

### 3.3.3 Analysis

The purpose of the seven channel model is to observe how the pressure drop through the channels changes with respect to the varying boundary conditions. Since the center channel is designed to be the initiation point of the deflection, this is the area of greatest interest. Therefore the center channel and the two neighboring channels are the primary focus of this study. In order to clearly distinguish between the channels each channel has been assigned a letter as shown in Figure 3.6.
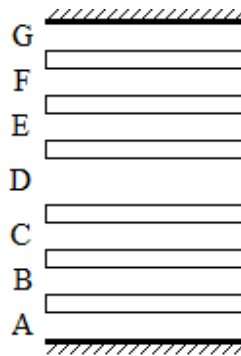


Figure 3.6: Letters used to distinguish channels

The height of Channel D is 0.125 inches and all other channels have a height of 0.075 inches for every *case*.

To analyze these channels the Middle Middle line probe from Figure 3.2 was used to find the pressure and the velocity through Channels C, D, and E. The five line probes from Figure 3.4 were used in each of these three channels to collect velocity profile data. Finally a plane was drawn in the same quarter width location as the five line probes from Figure 3.4 and is shown in Figure 3.7.
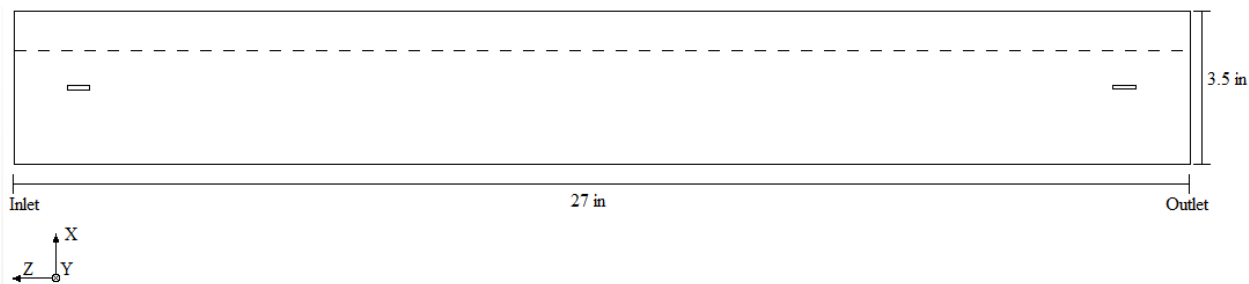
Figure 3.7: Pressure profile plane at a quarter of channel width

Further data was required for an accurate comparison between Miller's critical velocity from Equation (3.7) which is explained in the following section. For these comparisons velocity data needed to be taken about half way between the support comb and the side of the channel on each side of the support comb. A total of 6 additional line probes were created and are shown in Figure 3.8. These probes were also used to collect pressure data which was used to determine the net pressure acting on the plate.
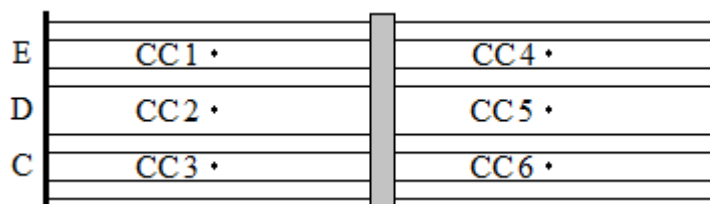


Figure 3.8: Six line probes for case comparison

The vertical bar in the center of the Figure represents the support comb. The dark lines on the edges of the channels indicate only the edge of the channel and are not intended to give edge support information.

## 3.4 Deflection Comparison

To determine if the data generated using Star-CCM+ is an accurate representation of what is to be expected in the experimental analysis the velocities from Star-CCM+ were compared with Miller's critical velocity equation for the appropriate boundary conditions. The equation presented in Section 2.1 was derived using fixed boundary

conditions. The plates within the GTPA are pinned, or simply-supported. Also Miller's equation is best used at the inlet of the flow channel. The inlet of the GTPA is stiffened by the addition of a support comb. This comb represents a clamped boundary condition. Therefore the boundary conditions used to derive Miller's velocity for this study were F-SS-F-C. By using these boundary conditions the span-width is reduced by half for this calculation due to the support comb being located in the span width center of the channel. The downstream side of the plate is not technically free since it is influenced by the continuation of the fuel plate. However, it will be assumed to be free for this approximation. Wide beam theory, which is used when the depth of the beam is three times larger than the thickness, was also used in this derivation.

The deflection of the beam relative to the edge supports for the given F-SS-F-C boundary conditions is given by the following equation.

$$y = \frac{p\left(1-v^2\right)\left(2x^4 - 5bx^3 + 3b^2x^2\right)}{48EI} \tag{3.5}$$

Following the same steps outlined in Section 2.1 the equation for the total change in cross section area divided by the original cross sectional area is obtained.

$$\frac{\Delta S}{S} = \frac{3p\left(1-v^2\right)b^4}{40Ea^3h} \tag{3.6}$$

The pressure differential derived from Bernoulli's equation is the same for this case as it was for the case outlined in Section 2.1. Therefore, by substituting Equation (3.6) into Equation (2.3) gives the critical velocity equation for the current study.

$$V_c = \sqrt{\frac{20gEa^3h}{3\rho b^4\left(1-v^2\right)}} \tag{3.7}$$

This equation is very similar to the equation derived using the F-C-F-C boundary conditions. The only difference is that the value multiplied to the variables within the square root is 20/3 instead of 15.

If the velocities generated using Star-CCM+ are greater than or equal to this critical velocity then the plate is expected to buckle. If they are smaller than this critical velocity measurable deflection is not expected to occur.

# 4    RESULTS AND DISCUSSION

All results presented in this chapter were produced by Star-CCM+ version 5.04.008.

## 4.1    One Channel Model

The objective of the results presented for the one channel model was to determine the mesh type, mesh size, and turbulence model approach. To do this, data was collected using the nine line probes from Figure 3.2. The results were used to make the necessary selections.

### 4.1.1  Mesh Type

To determine the mesh type that would be used for the two channel and seven channel analysis, data from the polyhedral and tetrahedral mesh types was compared and analyzed.

For model numbers that reflect coarse mesh sizes, some cells were so coarse the same data value was collected multiple times in a single cell. Also for Model 1.5 the Middle Middle line probe was not able to generate a full set of data points. These missing data points were not a problem for any other model. An example of both of these issues is shown in Figure 4.1.
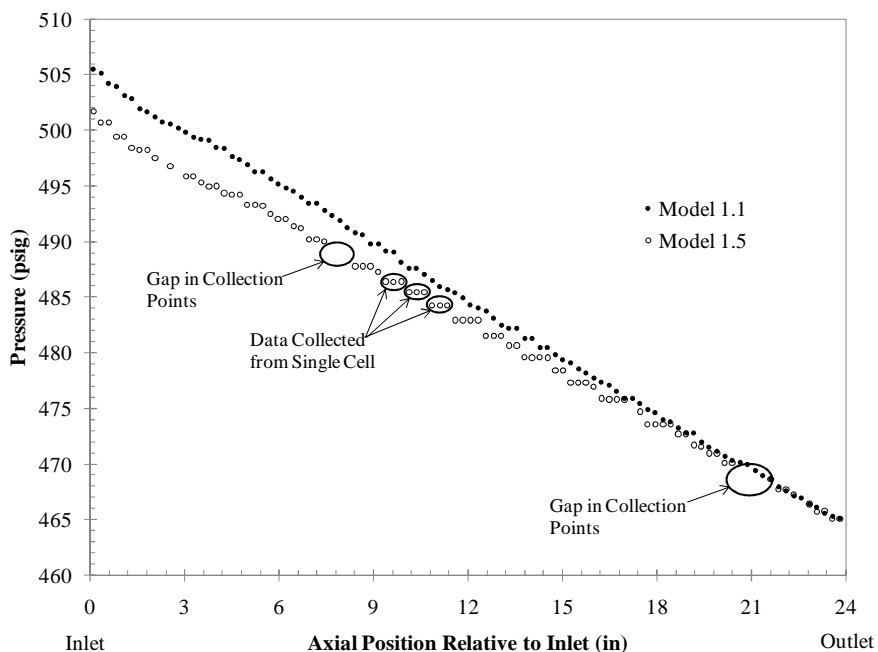
Figure 4.1: Example of data issues in coarse mesh for pressure comparison along Middle Middle line probe for Models 1.1 and 1.5

The graph shows that from approximately axial position 7.5 inches to axial position 8.5 inches there are missing data points in Model 1.5 as a result of an incomplete number of data collection points. There is another section of missing data points in Model 1.5 around axial position 20.5 inches to axial position 21.5 inches. Each of these instances are noted on the graph. There are a few other instances that are harder to see from this graph. Both data sets show signs of repeated data points as a result of multiple collection points in a single cell. These can be seen where the data seems to have two or more data points that are on the same y-axial location and a few of them are labeled on the graph.

In order for the accurately compare two data sets there needs to be a point by point comparison. Therefore all data points that were missing from Model 1.5 were removed from Model 1.1. Also, since the duplicate data points cannot provide an accurate comparison, these were also removed along with the associated data point from the other data set. The result is shown in Figure 4.2.
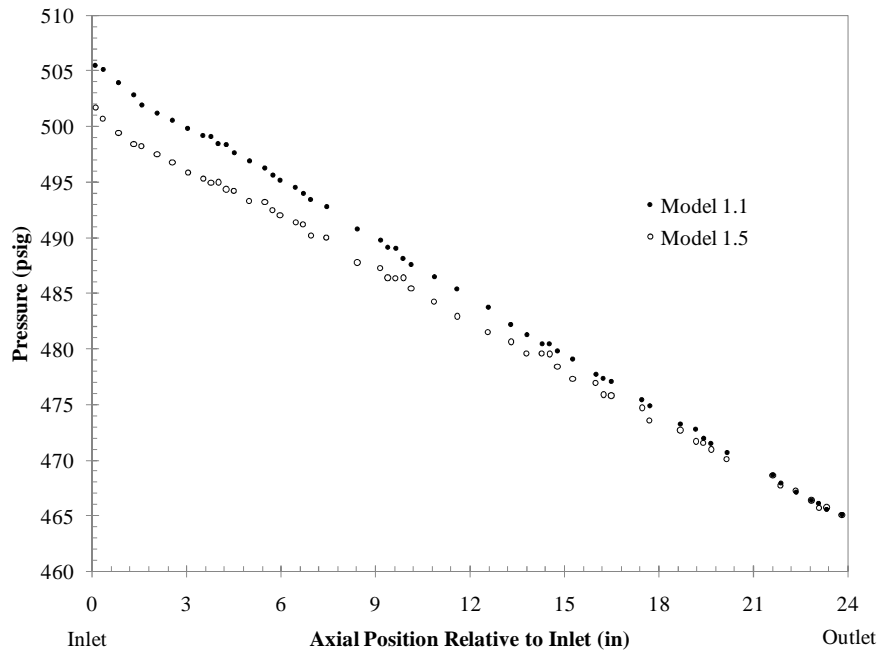
Figure 4.2: Corrected coarse mesh for more accurate comparison of pressure along
Middle Middle ling probe for Models 1.1 and 1.5

This same process of removing duplicate data points was performed on all data that
had such problems.

The comparisons of the other models for the mesh type analysis are shown in Figure
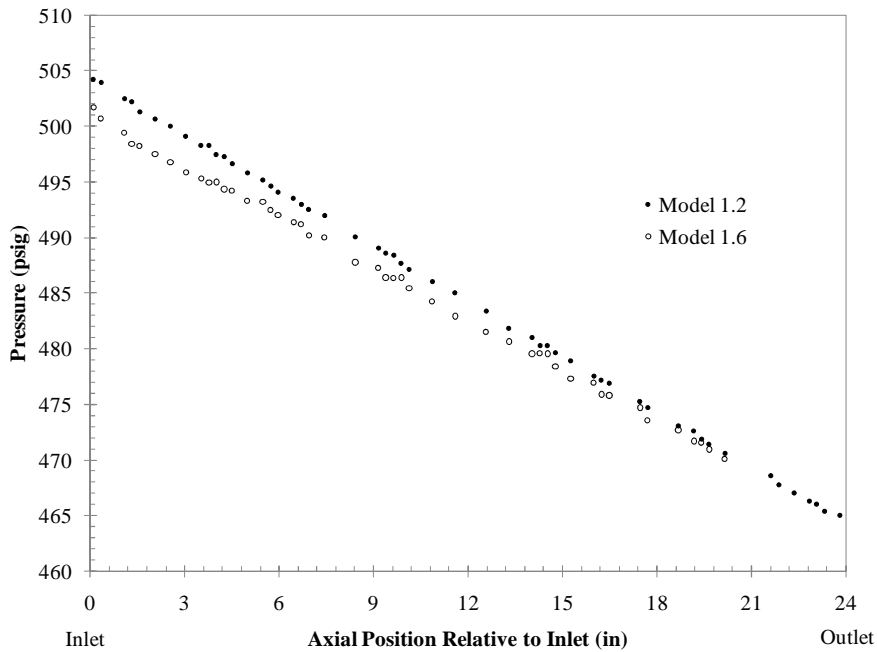4.3 and Figure 4.4.

Figure 4.3: Pressure comparison along Middle Middle line probe for Models 1.2 and 1.6
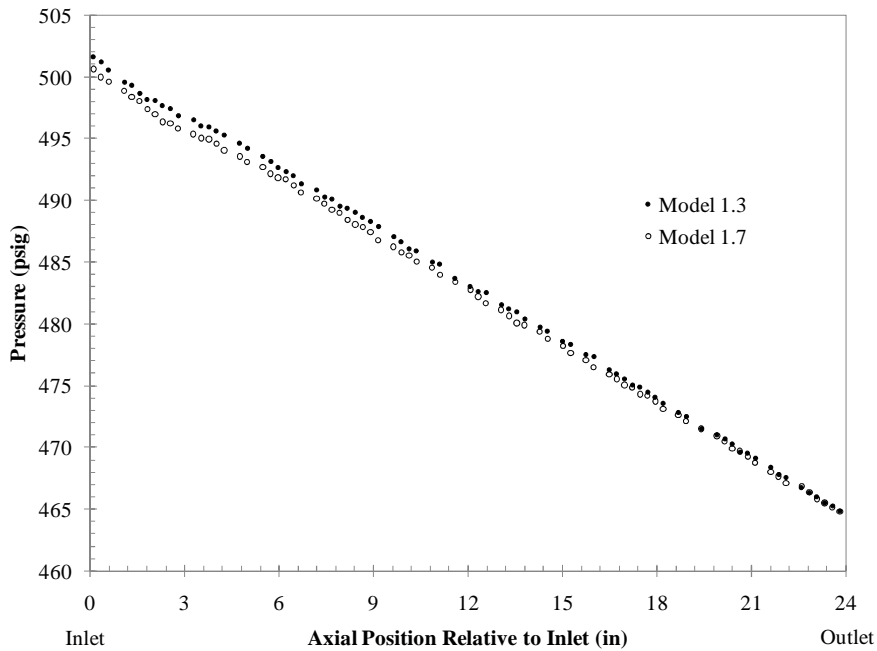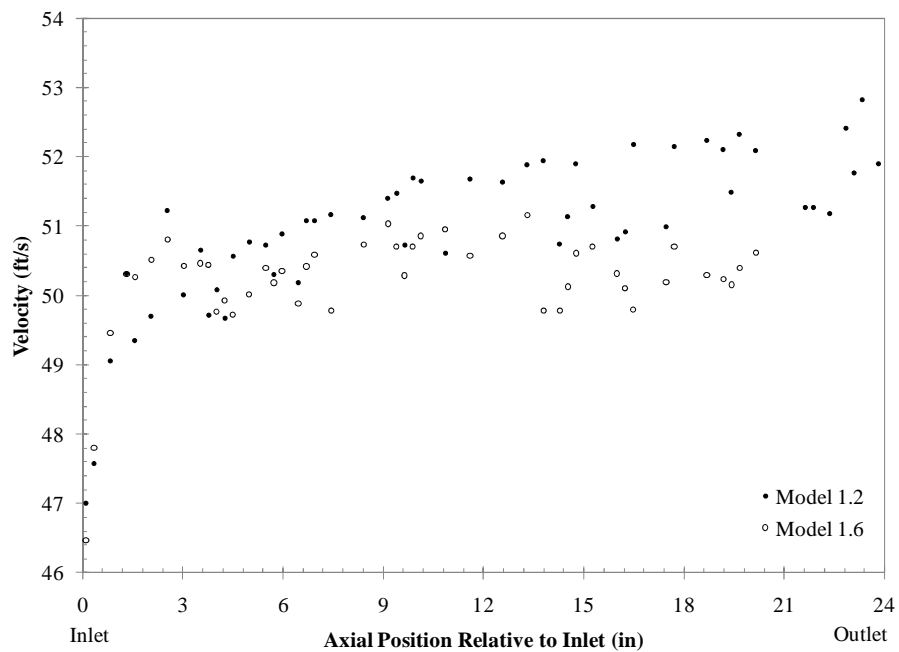


Figure 4.4: Pressure comparison along Middle Middle line probe for Models 1.3 and 1.7

Figure 4.3 shows that the data produced using the RSM approach is slightly closer than the data produced using the k-ε approach shown in Figure 4.2. Figure 4.4 shows that the data produced using RL 2 matches more closely than the data produced using RL 1 as shown in Figure 4.2.

The velocity through the channel is also analyzed along the same line probe. The plots of this data are shown below.
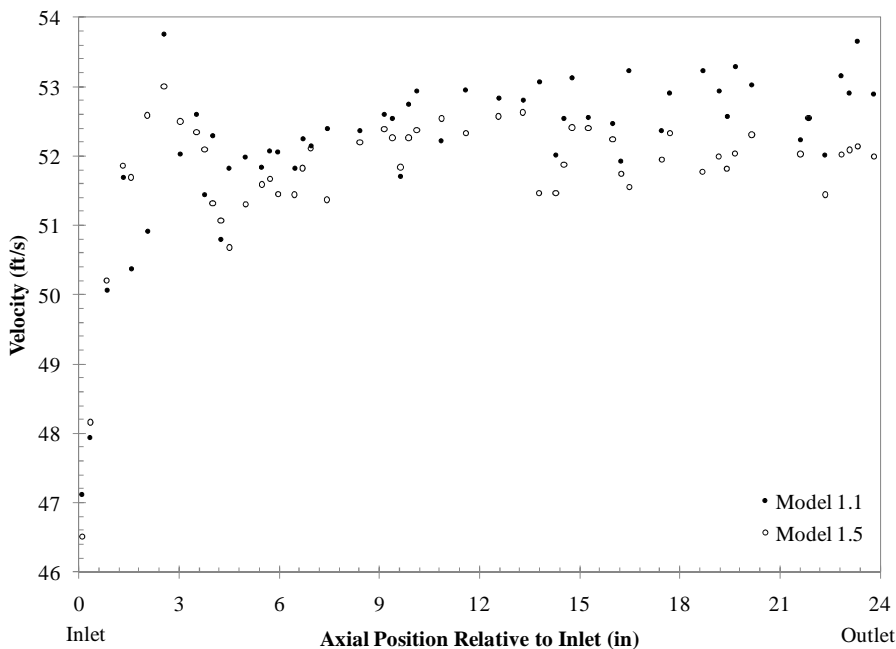


Figure 4.5: Velocity comparison along Middle Middle line probe for Models 1.1 and 1.5

Figure 4.6: Velocity comparison along Middle Middle line probe for Models 1.2 and 1.6
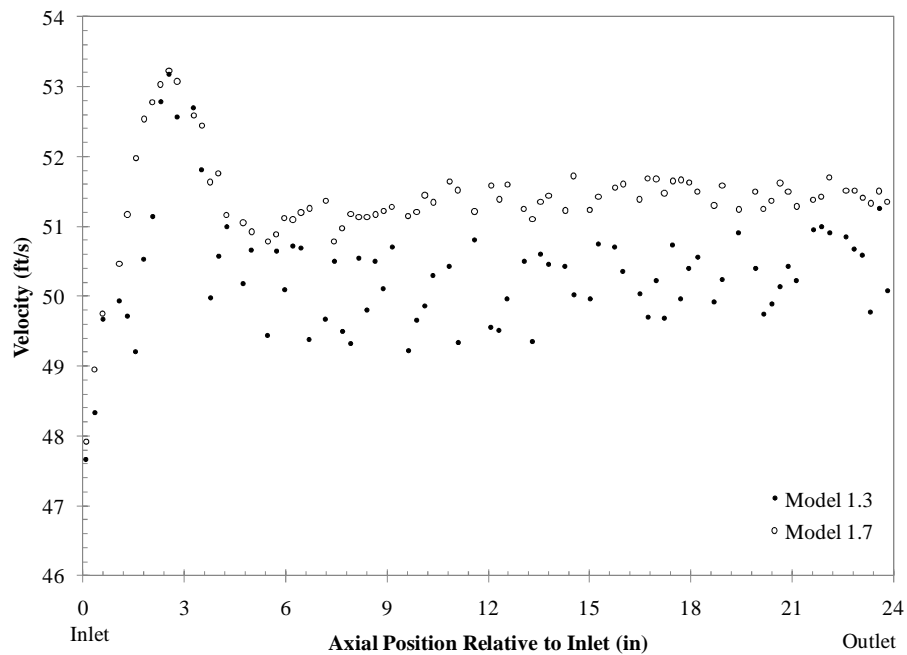


Figure 4.7: Velocity comparison along Middle Middle line probe for Models 1.3 and 1.7

The data shown in the velocity plots is scattered and difficult to discern. The reason the data is so scattered is because the coarseness of the mesh yields an inaccurate solution. The velocity plots at more refined mesh sizes do not have as much scatter. Because of the scatter it is difficult to make comparisons using these graphs. One observation from these figures is that the velocity at the inlet is much lower than the velocity through the rest of the channel. This is likely because the velocity is not yet fully developed at the inlet causing the inlet velocity to be lower than the rest of the channel.

It is difficult to draw firm conclusions by only looking at the graphs. Therefore the results from the percent difference analysis are presented in Table 4.1. These results support the behavior that was observed in the figures. The data between the polyhedral mesh type and the tetrahedral mesh type began to match more closely with the RSM approach as well as with a finer mesh refinement level.

Table 4.1: Mesh type % difference results

| Location (axial-, spanwise-position) | % Difference Value | | |
|---|---|---|---|
| | Model 1.1 vs. Model 1.5 | Model 1.2 vs. Model 1.6 | Model 1.3 vs. Model 1.7 |
| Bottom Left | 0.496 | 0.265 | 0.145 |
| Bottom Middle | 0.464 | 0.242 | 0.145 |
| Bottom Right | 0.530 | 0.301 | 0.140 |
| Middle Left | 0.457 | 0.243 | 0.148 |
| Middle Middle | 0.446 | 0.214 | 0.128 |
| Middle Right | 0.437 | 0.222 | 0.155 |
| Top Left | 0.467 | 0.244 | 0.130 |
| Top Middle | 0.449 | 0.232 | 0.146 |
| Top Right | 0.478 | 0.254 | 0.142 |

This data indicates that the pressure results for the two models matches fairly close with each comparison being less than one percent. Models 1.1 and 1.5 Models, which used RL 1 and the k-ε turbulence model approach, have the least alike data sets.

Models 1.2 and 1.6, also used RL 1 but used the RSM approach instead of the k-ε approach, match closer than the Models 1.1 and 1.5. Furthermore, a finer mesh size, as was used in Models 1.3 and 1.7 with RL 2 and a k-ε approach, produces results that indicate a better match than either of the other two comparisons.

The results indicate that it does not matter which mesh type is used for this analysis because all comparisons match closely. However, RL 3 is the smallest refinement level that the tetrahedral mesh was able to compute under the given input data. Therefore, the polyhedral mesh was selected because of the ease in processing further refinement levels as well as the supporting data that indicates that at the finer refinement levels the two mesh types would be fairly similar.

## *4.1.2  Turbulence Model Approach*

In order to determine if the k-ε approach could justifiably be used in place of the RSM, as was mentioned in Section 3.1.5, the results from three different refinement levels were analyzed as shown in Table 3.6. At each refinement level the data from the k-ε and RSM approaches were compared. The input parameters for each comparison were identical except for the turbulence model approach and the physics models associated with each approach as outlined in Table 3.7.

As was done with the previous analysis, the pressure drop for each comparison was plotted and analyzed as shown below.
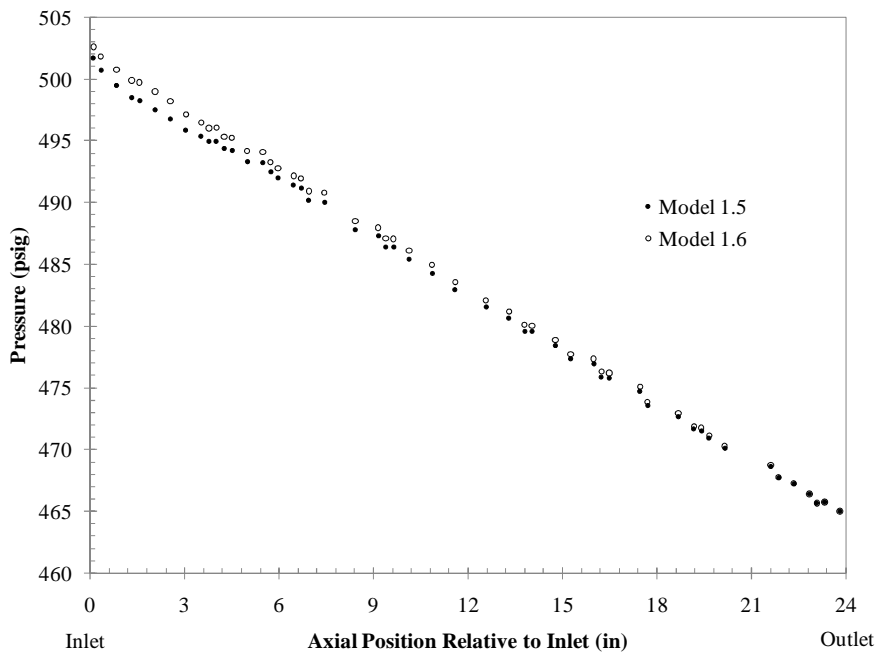
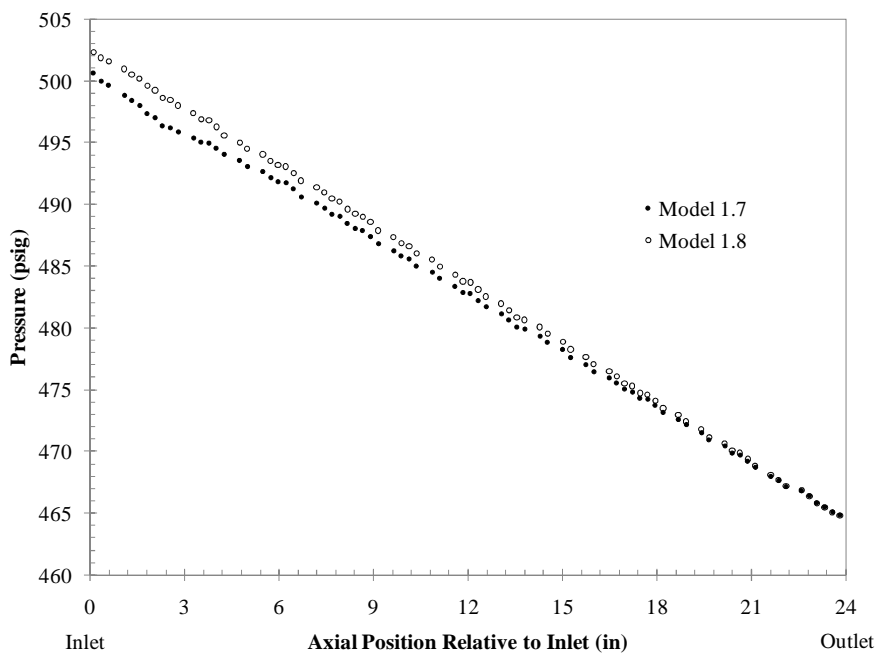Figure 4.8: Pressure comparison along Middle Middle line probe for Models 1.5 and 1.6



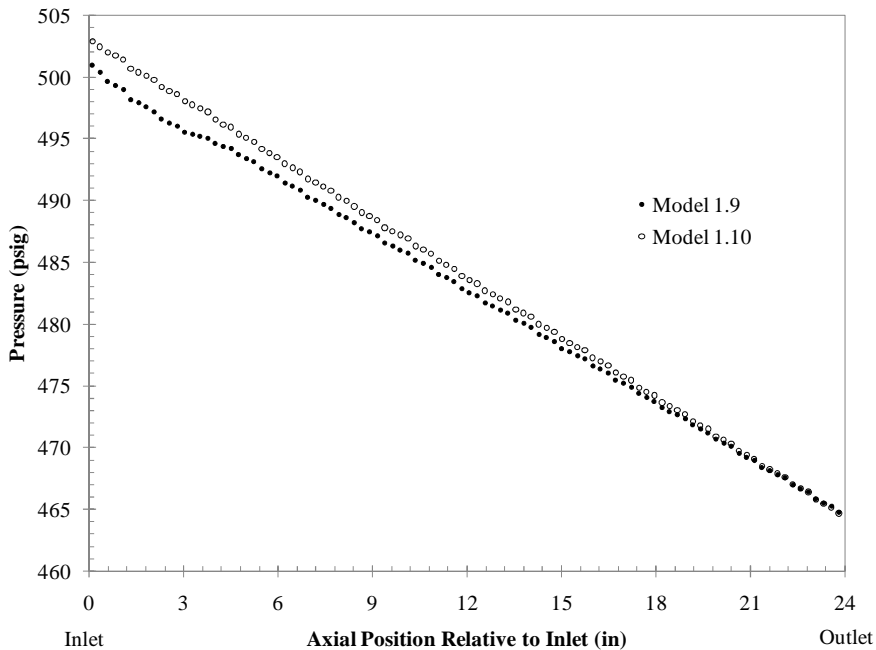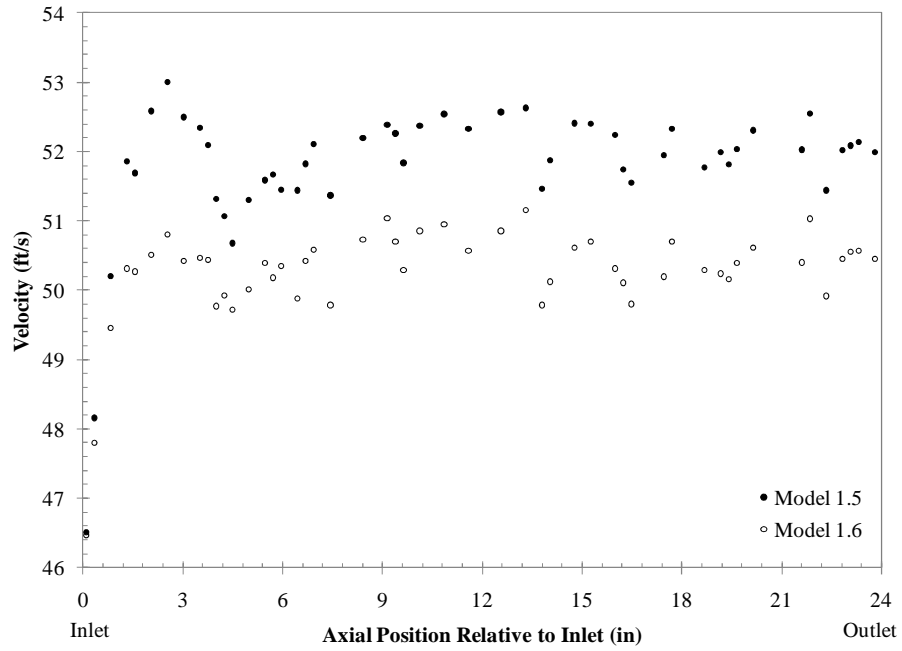Figure 4.9: Pressure comparison along Middle Middle line probe for Models 1.7 and 1.8

Figure 4.10: Pressure comparison along Middle Middle line probe for Models 1.9 and 1.10

Although the data in each graph seems to match fairly closely, it can be seen that as the refinement level increases the data sets become farther and farther apart. The velocity data was also collected along the Middle Middle line probe and yielded similar results.

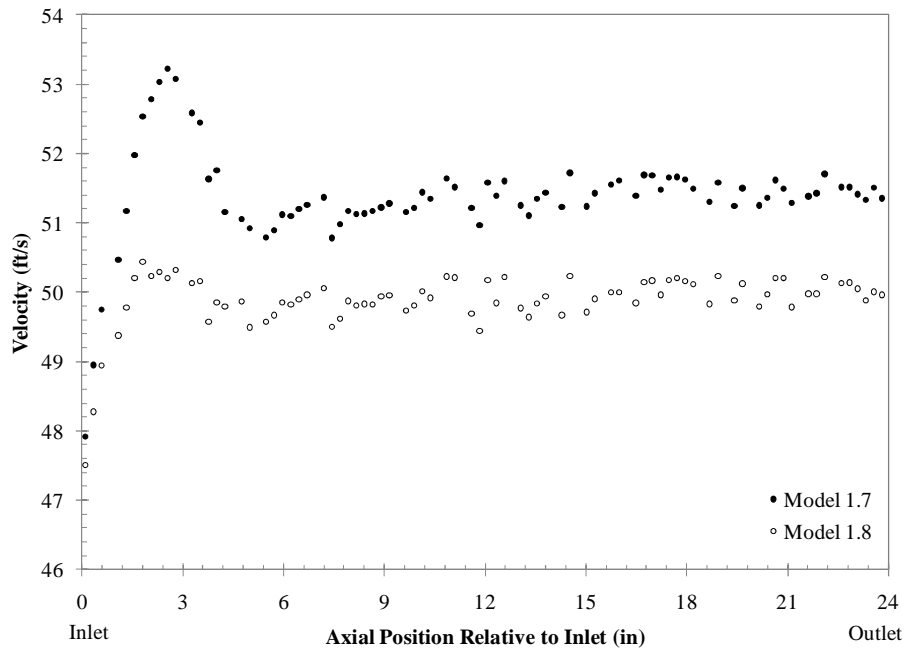Figure 4.11: Velocity comparison along Middle Middle line probe for Models 1.5 and 1.6



Figure 4.12: Velocity comparison along Middle Middle line probe for Models 1.7 and 1.8
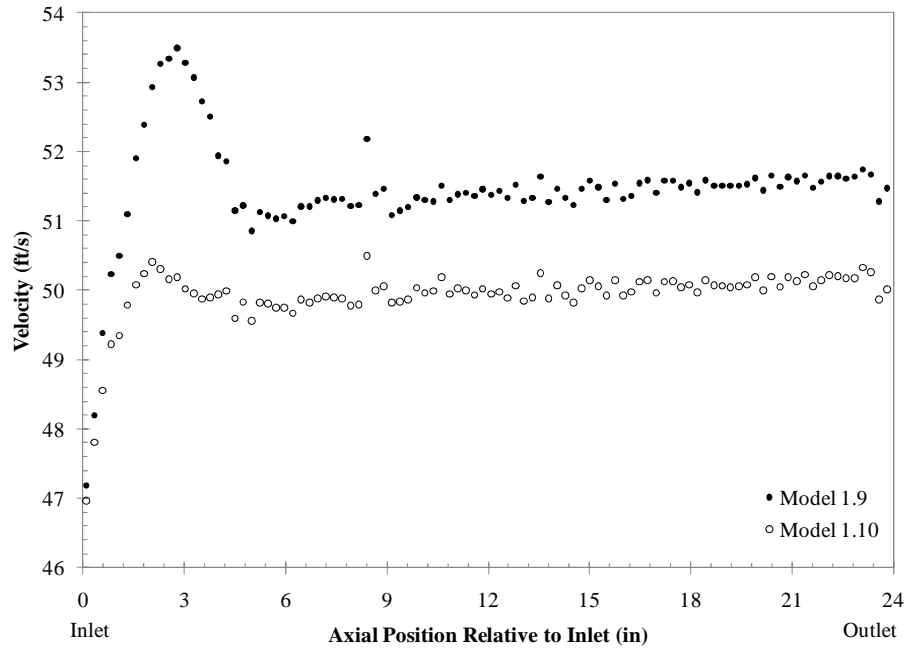
Figure 4.13: Velocity comparison along Middle Middle line probe for Models 1.9 and 1.10

Although it is difficult to see in the graph, the data in Figure 4.13 is farther apart than the data in Figure 4.11 and Figure 4.12. Since this is difficult to determine using the graphs percent difference method was again used to determine the similarity for each comparison and the results are shown in Table 4.2.

Table 4.2: Turbulence model approach % difference results

| Location (axial-, spanwise-position) | % Difference Value | | |
|---|---|---|---|
| | Refinement Level 1 | Refinement Level 2 | Refinement Level 4 |
| Bottom Left | 0.124 | 0.189 | 0.217 |
| Bottom Middle | 0.114 | 0.186 | 0.216 |
| Bottom Right | 0.123 | 0.19 | 0.218 |
| Middle Left | 0.117 | 0.199 | 0.217 |
| Middle Middle | 0.130 | 0.196 | 0.222 |
| Middle Right | 0.118 | 0.177 | 0.215 |
| Top Left | 0.121 | 0.190 | 0.217 |
| Top Middle | 0.118 | 0.186 | 0.222 |
| Top Right | 0.124 | 0.19 | 0.217 |

The results indicate that as the refinement level becomes finer, and thus produce a more precise result, the two data sets became more unique. Initially the comparisons made using the T-test indicated that the results from the RL 4 comparison was too unique to justifiably use the k-ε model in place of the RSM model therefore the RSM model was selected. However, this since the percent difference method produces results that are all lower than one percent it seems that, perhaps, the k-ε model could have been used. This may not be true at finer mesh sizes since the data does indicate that with a more refined mesh the data from the two models becomes more unique. Therefore, a future analysis could be conducted to test the k-ε model at the refinement level that generates a grid independent solution.

## *4.1.3  Grid Refinement*

For the grid sensitivity study the data taken along the Middle Middle line probe was plotted and analyzed. The plots give good indication that a grid independent solution has been achieved. The plots representing the pressure drop through the channel are shown below.
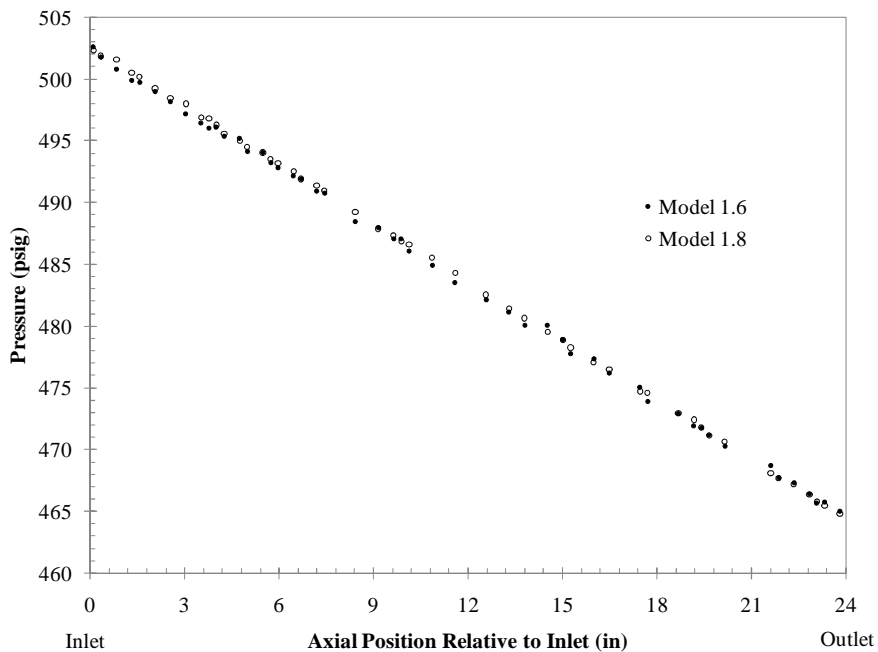
Figure 4.14: Pressure comparison along Middle Middle line probe for Models 1.6 and 1.8
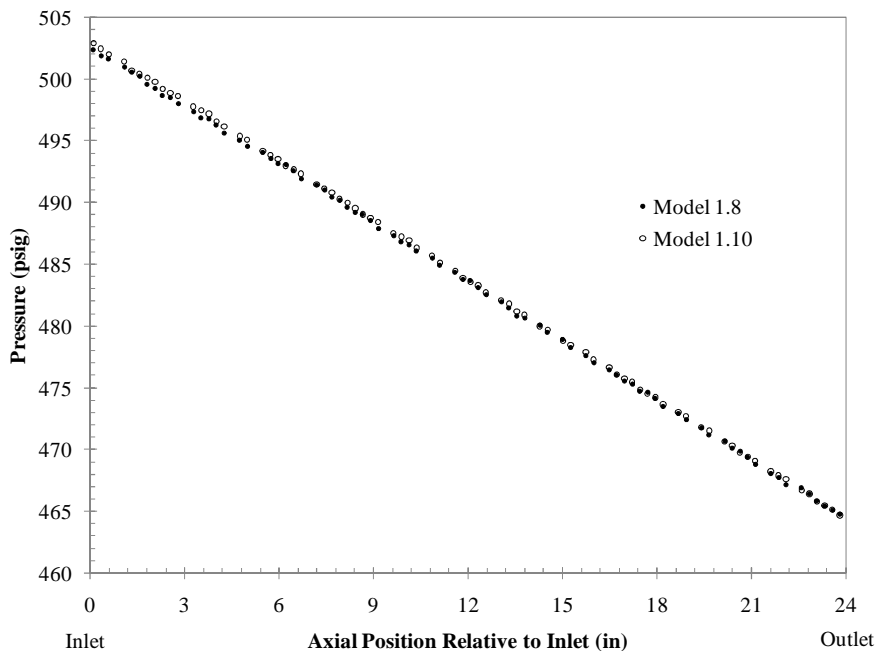


Figure 4.15: Pressure comparisons along Middle Middle line probe for Models 1.8 and 1.10
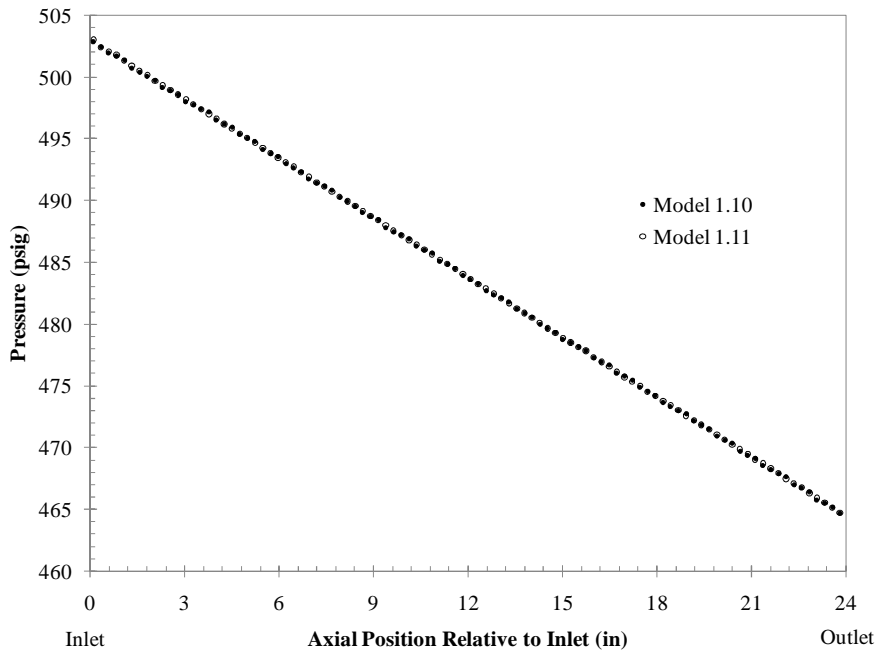
Figure 4.16: Pressure comparison along Middle Middle line probe for Models 1.10 and 1.11

The pressure plot comparing Model 1.10 with Model 1.11 seems to indicate that Model 1.11 is good data with no visual issues. However, the velocity plot has an unstable oscillation that could not be resolved as shown in Figure 4.20. Therefore, Model 1.10 and Model 1.12 were also compared to ensure that they were also a good match of data. This comparison is shown in Figure 4.17.
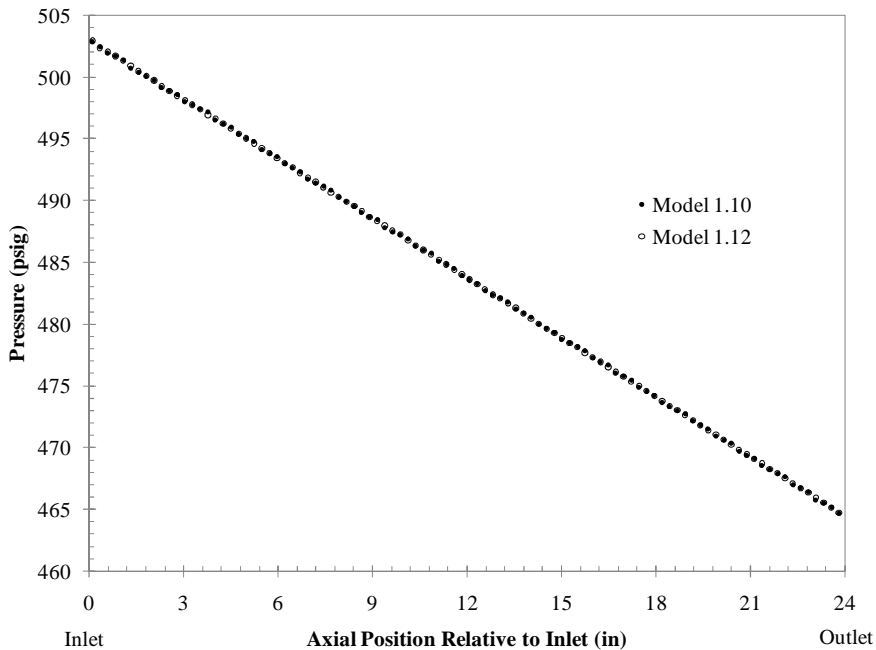
Figure 4.17: Pressure comparison along Middle Middle line probe for Models 1.10 and 1.12

The figures show that for each comparison the two data sets are fairly similar but that the comparison of Models 1.10 and 1.12 matches more closely than the rest.

The velocities for the grid refinement study are also plotted using the same line probe as were used for the pressure plots.
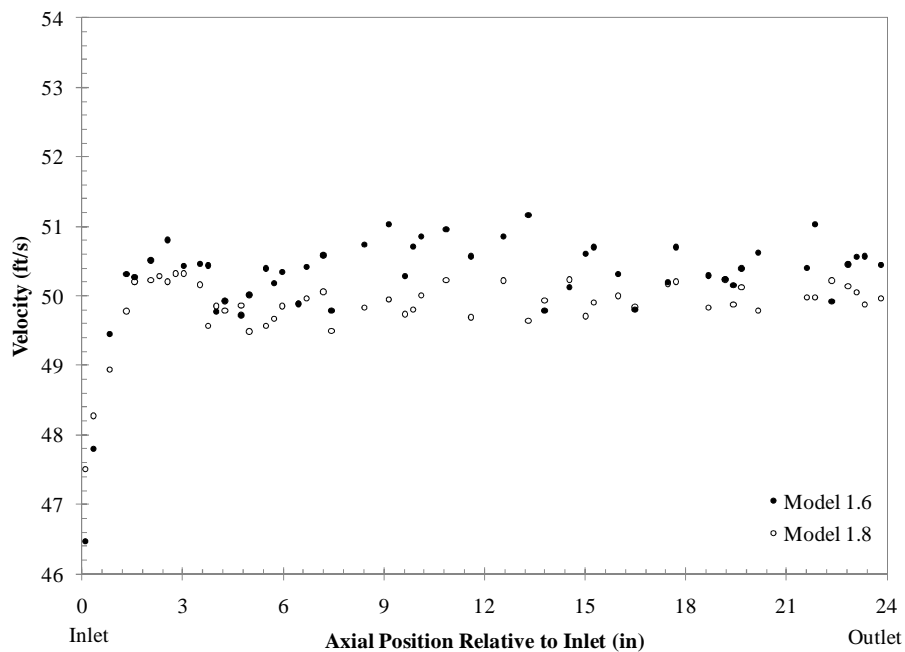
Figure 4.18: Velocity comparison along Middle Middle line probe for Models 1.6 and 1.8
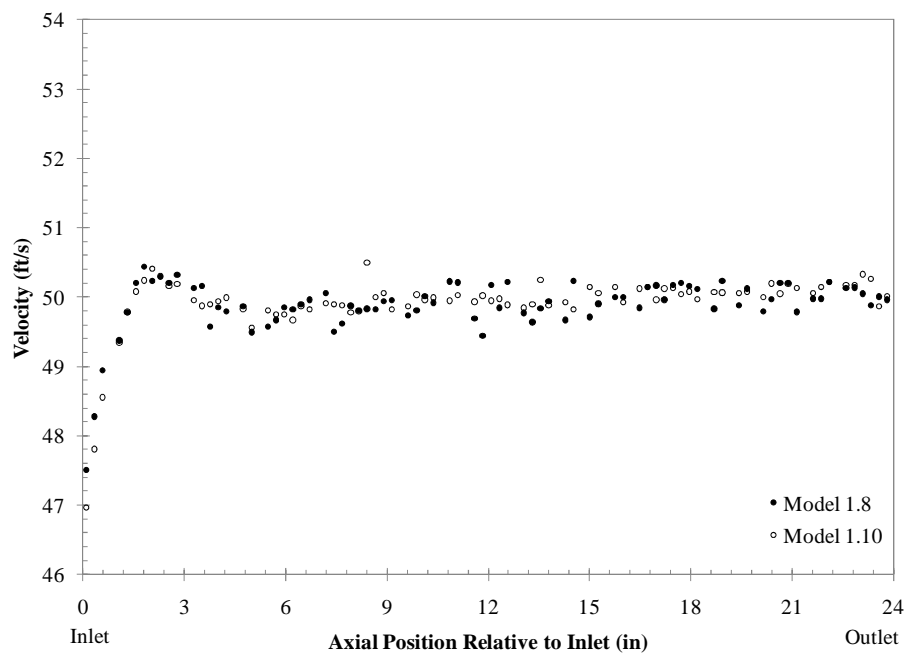


Figure 4.19: Velocity comparison along Middle Middle probe for Models 1.8 and 1.10
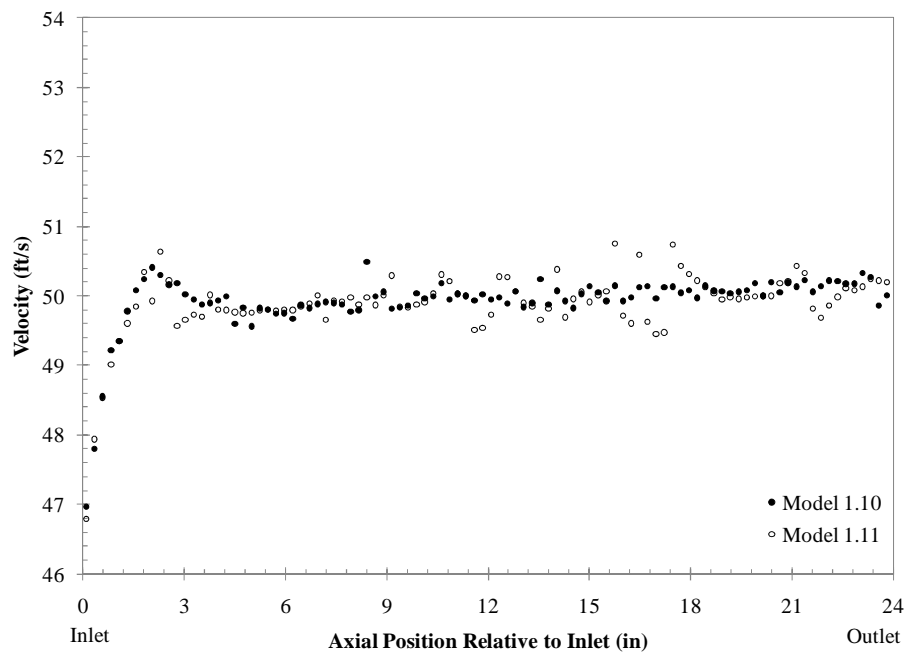
Figure 4.20: Velocity comparison along Middle Middle probe for Models 1.10 and 1.11

Figure 4.20 shows the unstable oscillation in Model 1.11 that was mentioned previously. Because of this oscillation the data produced from this simulation is not valid and another refinement level, RL 6, was analyzed in order to achieve a grid independent solution.
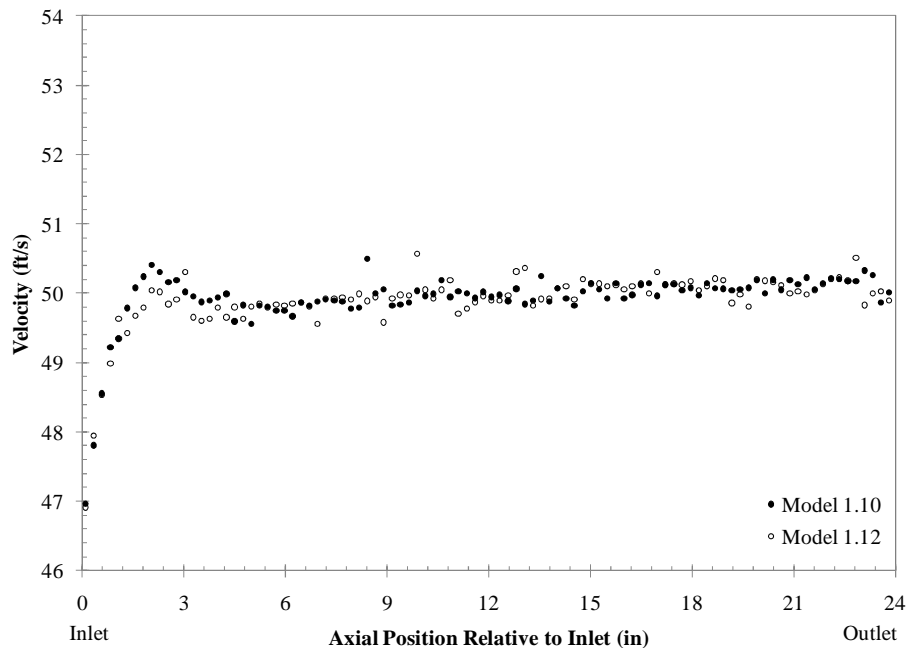
Figure 4.21: Velocity comparison along Middle Middle probe for Models 1.10 and 1.12

Figure 4.21 shows that the results of RL 4 and RL 6 match fairly closely with no evidence of unstable oscillations.

The percent difference analysis of this data as shown in Table 4.3 supports the results indicated from the figures.

Table 4.3: Grid sensitivity study % difference results

| | | % Difference Value | | |
| --- | --- | --- | --- | --- |
| Location (axial- spanwise-position) | RL 1 vs. RL 2 | RL 2 vs. RL 4 | RL 4 vs. RL 5 | RL 4 vs. RL 6 |
| Bottom Left | 0.108 | 0.059 | 0.017 | 0.017 |
| Bottom Middle | 0.091 | 0.058 | 0.016 | 0.016 |
| Bottom Right | 0.134 | 0.054 | 0.016 | 0.016 |
| Middle Left | 0.137 | 0.074 | 0.009 | 0.011 |
| Middle Middle | 0.070 | 0.050 | 0.015 | 0.015 |
| Middle Right | 0.097 | 0.085 | 0.017 | 0.018 |
| Top Left | 0.136 | 0.054 | 0.019 | 0.020 |
| Top Middle | 0.104 | 0.056 | 0.016 | 0.017 |
| Top Right | 0.087 | 0.065 | 0.017 | 0.017 |

These results indicate that pressure results are all very close with one another. Initially RL 5 was selected as the grid independent solution because, even with the T-test, the data matches very closely between those two refinement levels. However, RL 5 produced the unstable results in the velocity data and, thus, was no longer able to be used. Therefore RL 6 was created and compared again with RL 4. The data matches just as well as the comparison between RL 4 and RL 5 and there were no observable oscillations in the velocity for RL 6.

To check to ensure that this was within the uncertainty of the solution the Richardson Extrapolation technique, described in Section 3.1.8, was used to calculate the uncertainty for the solution generated using RL 6. The percent difference between the Richardson's Extrapolation value and the value of RL 6 is the uncertainty percent associated with the solution for RL 6. This value was normalized along with the percent difference between RL 4 and RL 6. The normalized values are shown in Table 4.4.

Table 4.4: Normalized values for uncertainty comparison

| Line Probe | RL 4 vs. RL 6 Norm | RL 6 vs. Richardson Extrapolation Norm |
|---|---|---|
| Bottom Left | 0.193 | 2.93 |
| Bottom Middle | 0.189 | 2.86 |
| Bottom Right | 0.188 | 2.84 |
| Middle Left | 0.128 | 1.94 |
| Middle Middle | 0.179 | 2.71 |
| Middle Right | 0.216 | 3.27 |
| Top Left | 0.232 | 3.52 |
| Top Middle | 0.213 | 3.23 |
| Top Right | 0.197 | 2.97 |

Since the normalized values for the grid sensitivity study comparison are lower than the values for the normalized values for the uncertainty this indicates that the refinement level 6 is, indeed, a grid independent solution.

### 4.1.4  Closing

The selections made as a result of the one channel analysis will be used for both the two channel and seven channel analysis as well. The polyhedral mesh type was selected and the approach was to solve the RANS turbulence model. Finally, RL 6 was selected as a result of the grid sensitivity study which was discussed in Section 4.1.3.

## 4.2   Two Channel Model

The purpose of the two channel model is to check the selections made from the one channel analysis to see if there are any obvious problems that need to be addressed before continuing on to the seven channel model analysis. The results presented here focus mainly on the pressure and velocity in each channel of the two channel model.

### 4.2.1  Pressure

The Middle Middle line probe was again used to collect data points in each of the two channels. The pressure drop for both channels is shown in Figure 4.22.
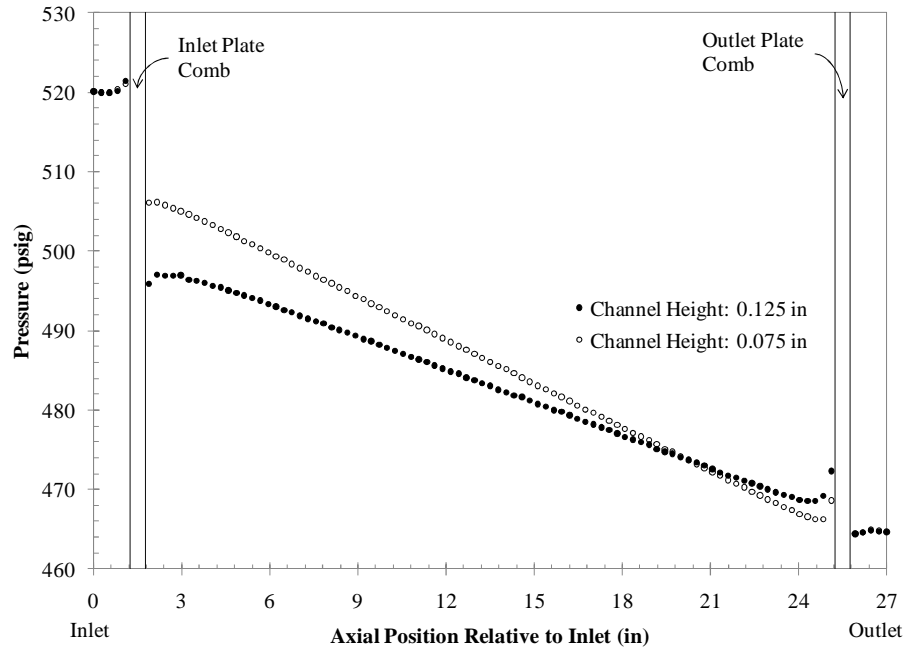
Figure 4.22: Pressure drop along Middle Middle probe for two channel model

The pressure in the small channel is higher immediately following the support comb as a result of the lower velocity in that channel. The pressure drop is larger in the small channel than the pressure drop in the large channel because of the smaller cross-sectional area and increase friction loss factor. As expected, the presence of the two mixing regions and the two support combs caused a significant effect on the pressure drop. It is important to note that, even in the two channel model, there is a significant pressure difference between the two channels which could lead to plate deflection.

## 4.2.2 Velocity

The velocity through the two channels was also taken along the Middle Middle line probe and the results are shown in Figure 4.23.
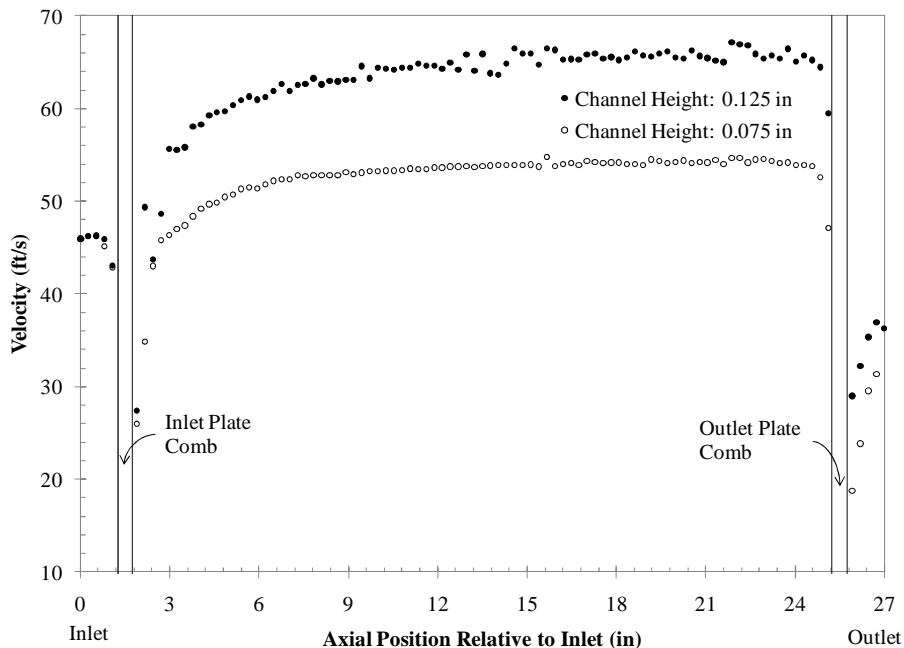
Figure 4.23: Velocity along Middle Middle line probe for two channel model

The support combs cause a significant drop in the velocity because at these points on the Middle Middle line probe the fluid is attempting to circumvent the support combs.

The data collected along the five line probes from Figure 3.4 are shown in Figure 4.24. It is interesting to note how the presence of the fuel plate affects the velocity profile for Probe 1.
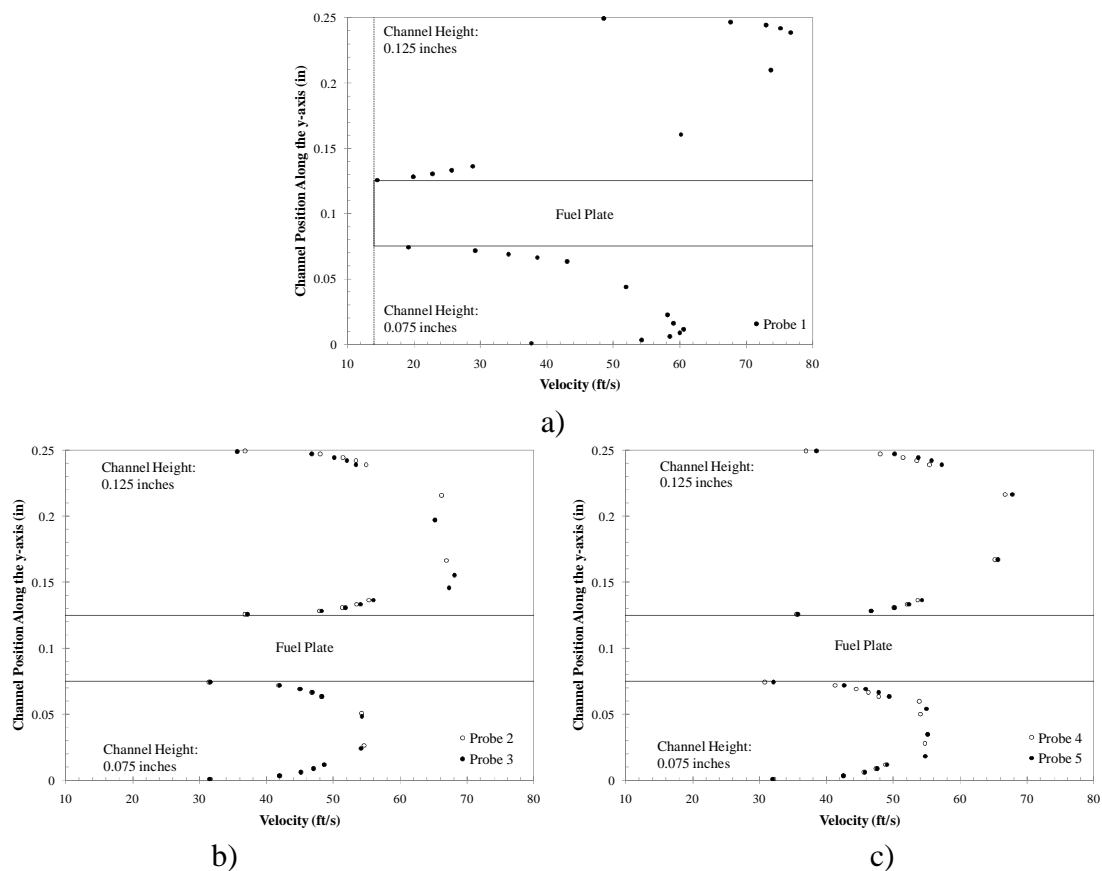
Figure 4.24: Velocity profiles for a) Probe 1, b) Probes 2 and 3, and c) Probes 4 and 5

Note that the x-axis in Figure 4.24 is velocity and not position. This causes some confusion in Figure 4.24 a) because the edge of the fuel plate indicates the location at which this data was taken relative to the image of the fuel plate. The dashed line is drawn at the location at which the velocity profile was collected in an attempt to clear up confusion. This same clarification technique is used on all similar images in the seven channel analysis.

The velocity for Probe 1 in each channel is significantly different than the rest of the velocities. This is due to its proximity to the point where the flow has just been separated by the fuel plate. The velocity next to the fuel plate slows significantly relative to the rest of the velocity in the channel. At 6 inches down the channel, Probe 2, the flow is fully developed. The velocity profile looks as expected for probes 4 and

5 and it is assumed that if there were more computational cells in the other regions that these would be more representative of turbulent flow.

It is important to note that in each figure the 0.075 inch channel has a slower velocity than the 0.125 inch channel. If the mass flow rates in the two channels were equal, then the 0.075 inch channel would have a faster velocity than the 0.125 inch channel. But, in this case the mass flow rate is larger in the 0.125 inch channel because of the lower loss coefficients associated with that channel. Because there are higher loss coefficients for the smaller channel most of the flow is diverted into the larger channel meaning that the 0.125 inch channel has a higher mass flow rate than the 0.075 inch channel leading to the higher velocity.

### 4.2.3  Closing

The results presented in the two channel indicate that there are no major concerns as a result of the criteria selected using the one channel model. Therefore, these same criteria will be used for the full seven channel model.

## 4.3   Seven Channel Model

The five cases presented in the seven channel model are intended to demonstrate the effect of varying boundary conditions on the pressure differential between the channels. The boundary conditions for each of the five cases are outlined in Table 3.17.

### 4.3.1  Case 1

The pressure drop for the three center channels along the Middle Middle line probe are shown in Figure 4.25.
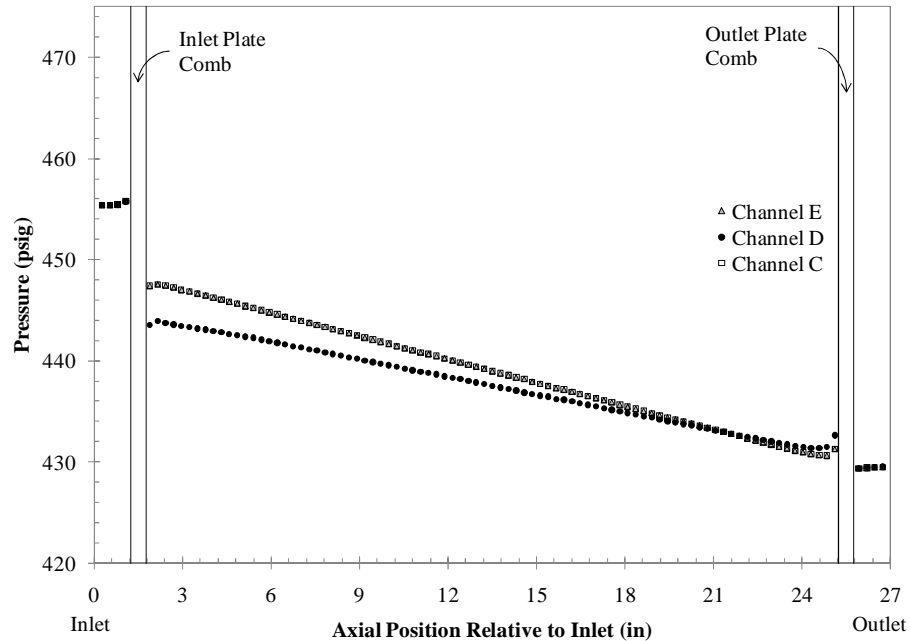
Figure 4.25: Case 1 pressure drop through the three center channels

The two channels bordering the center channel have such similar pressure drops that the data lies on top of one another. At the inlet of the channels the pressure difference is the largest. This is the same behavior that was observed in the two channel model results in Figure 4.22. Also the smaller side channels have a larger pressure drop through the fueled region than the center channel due to the difference in geometry between the channels. It is interesting to note that because the two smaller channels have a larger pressure drop than the larger center channel that at the outlet the center channel has a higher pressure than the two bordering channels.

The velocity through these three channels is shown in Figure 4.26.
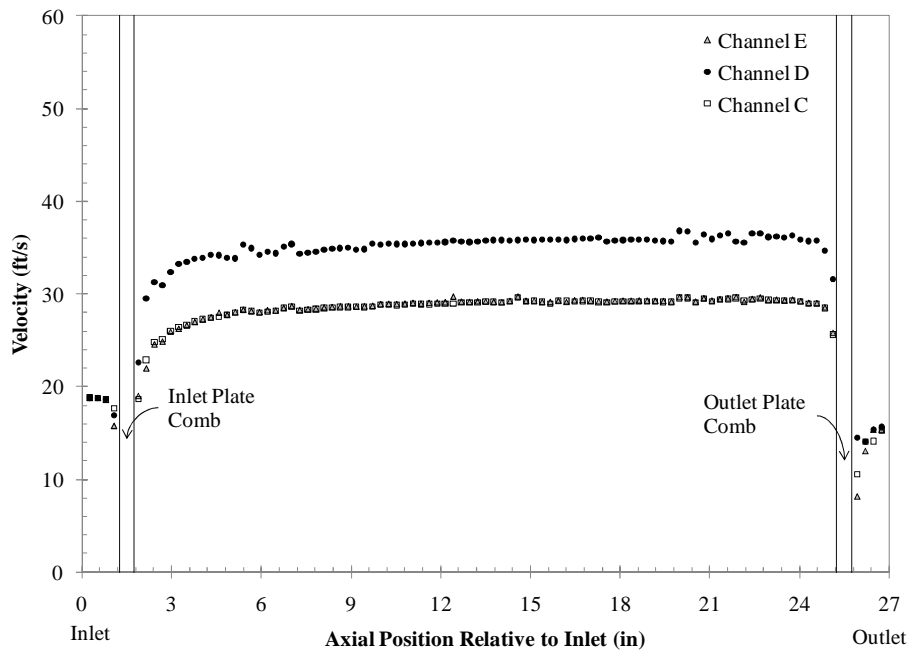
Figure 4.26: Case 1 velocity through the three center channels

In this model, as in the two channel model, the larger center channel has a higher velocity than the two bordering channels. The figure shows that the velocity slowly increases as it progresses through the channel and is affected greatly by the presence of the support comb.

The velocity profile data obtained from the five line probes shown in Figure 3.4 shows a similar behavior of the velocity as shown in Figure 4.27.
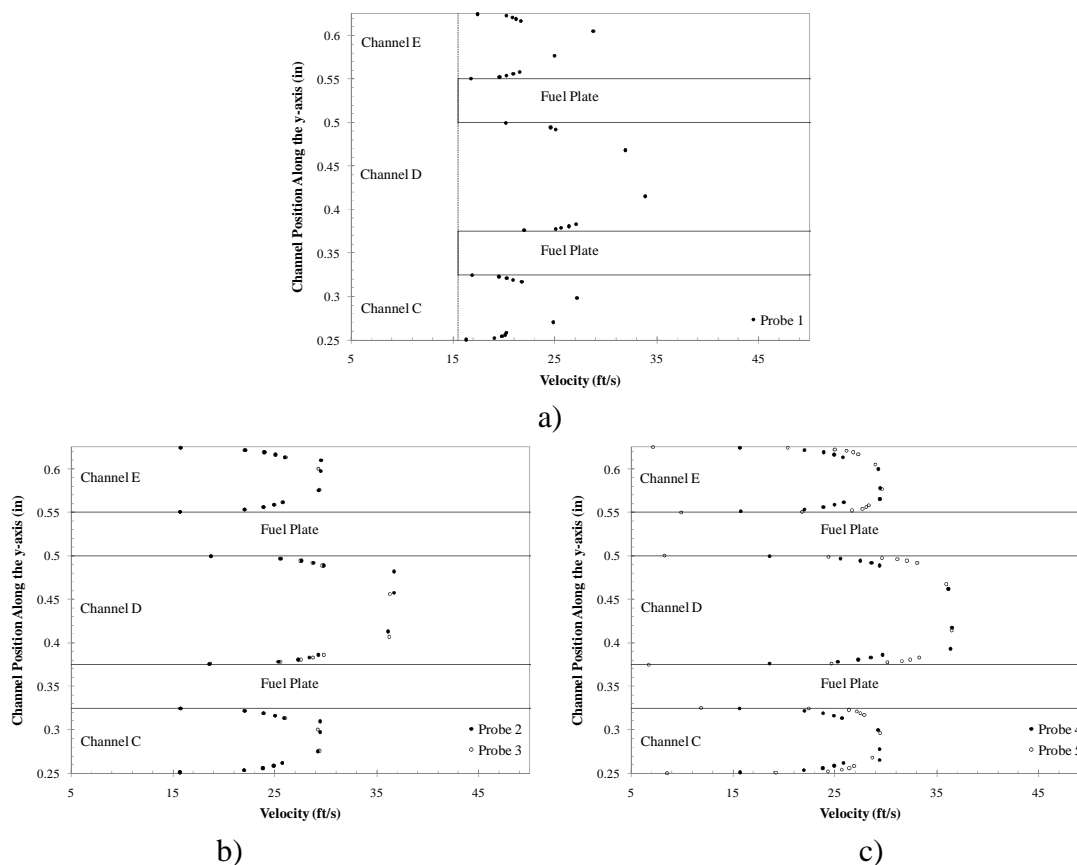
Figure 4.27: Case 1 velocity profiles for a) Probe 1, b) Probes 2 and 3, and c) Probes 4 and 5

Figure 4.27 a) shows that the flow is noticeably affected as it enters the channel keeping in mind that the dashed line is the location at which the velocity profile was obtained relative to the fuel plate. This behavior was also observed in the two channel model shown in Figure 4.24 a). However, the two channel model showed velocities that were very unbalanced. This unbalance was a result of the asymmetry of that model. Although the flow in the seven channel model is still noticeably unbalanced it is not as severe as the two channel model due to the flow which is diverted into the other channels which are not shown in the figure. The other parts of the figure, b) and c), show the same behavior observed in Figure 4.26 with the center channel having a faster velocity than the two bordering channels.

The pressure profile taken from the plane depicted in Figure 3.7 is shown in Figure 4.28
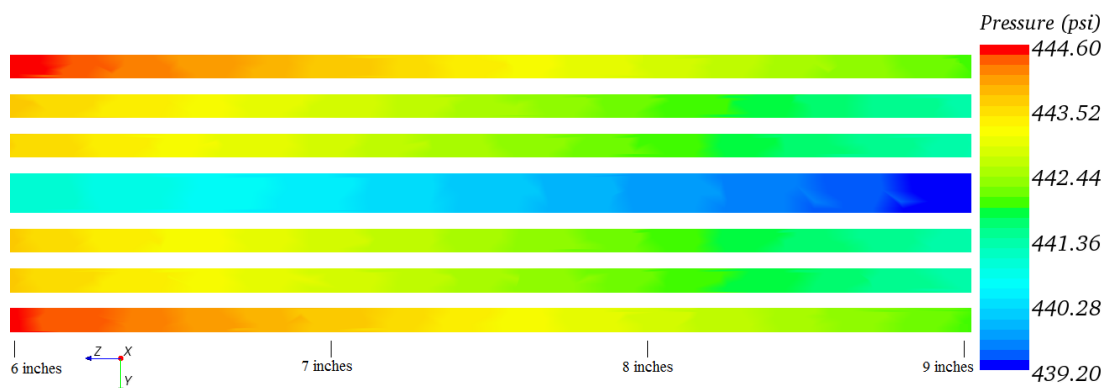


Figure 4.28: Case 1 pressure profile for all seven channels

Figure 4.28 shows the region of the assembly from six inches to nine inches. This region was focused on in each *case* because this is the region where maximum deflection is expected. The figure shows that the pressure in the center channel is noticeably lower than the pressure in each of the side channels. This figure also shows that the four channels closest to the center channel seem to have a similar pressure profile while the two outermost channels have the highest relative pressure than any of the other channels.

## 4.3.2  Case 4

The only difference between *Case 1* and *Case 4* is the inlet mass flow rate as a result of an increased volumetric flow rate. *Case 1* had a mass flow rate of 11.2 kg/s and *Case 4* had a slightly increased mass flow rate of 12.7 kg/s. This does cause a change in the results of the two *cases*. However, the difference is somewhat difficult to notice at first glance. It is important to look for inlet and outlet pressures and velocities as well as pressure and velocity differences between the channels in order to make any clear comparison of the data.

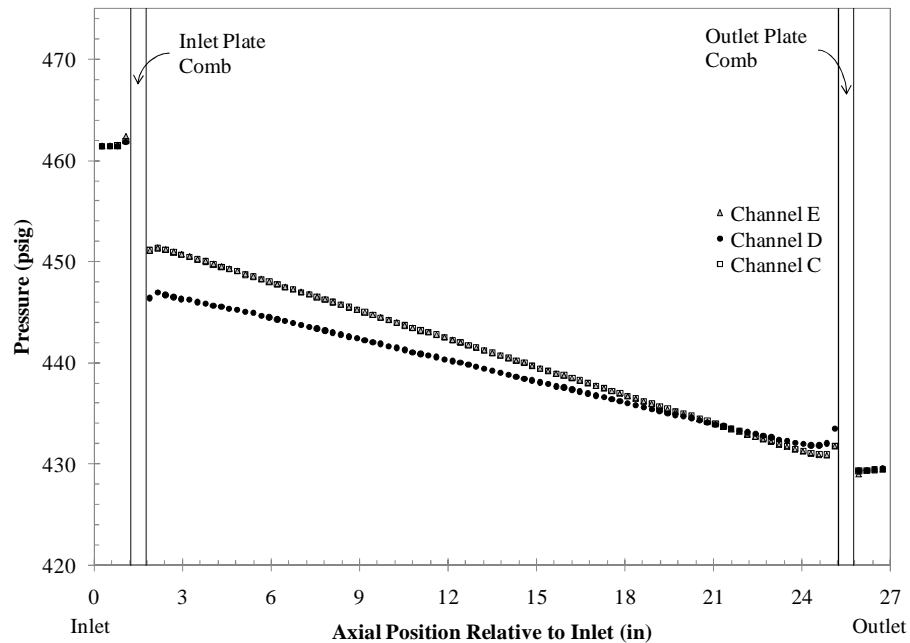The pressure drop for the three channels is presented in Figure 4.29.

Figure 4.29: Case 4 pressure drop through the three center channels

Notice that the difference between Figure 4.29 and Figure 4.25 is primarily the inlet pressure. *Case 1* has an inlet pressure around 455 psig where *Case 4* shows an inlet pressure of about 462 psig. The pressures in the channels are also different. *Case 1* has a center channel inlet pressure of about 444 psig and the two bordering channels each have an inlet pressure of close to 448 psig. Conversely *Case 4* has a center channel inlet pressure of 447 psig and the two bordering channels have an inlet pressure of about 452 psig. This shows about a 1 psig increase in the pressure differential at the inlet of the channel from *Case 1* to *Case 4*.

The velocity for *Case 4* as shown in Figure 4.30 is also different than the velocity presented in *Case 1*.
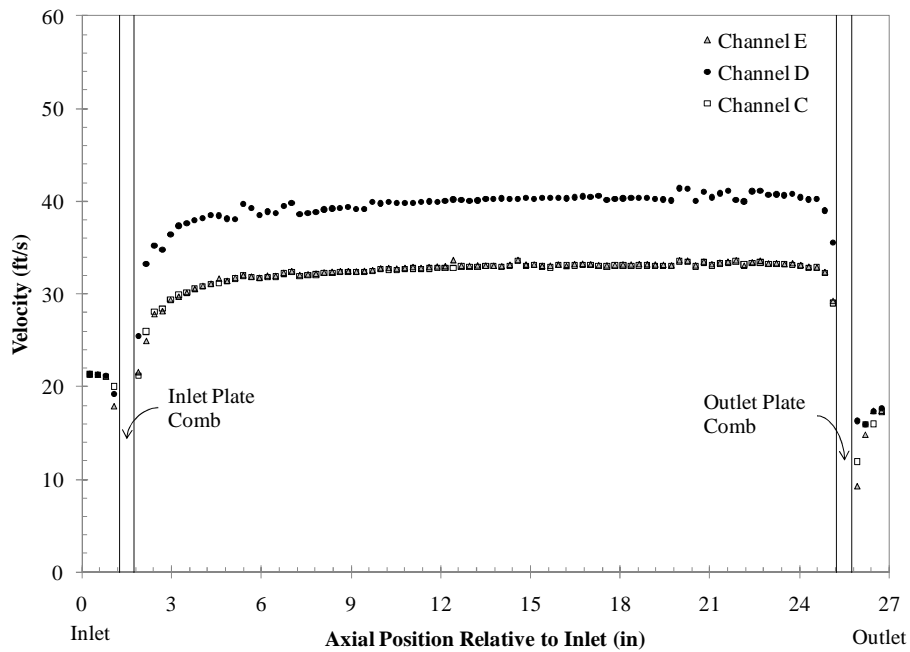
Figure 4.30: Case 4 velocity through the three center channels

The center channel velocity for *Case 4* is in the range of 38 to 40 ft/s whereas the velocity for the center channel in *Case 1* was closer to 34 to 36 ft/s. The difference between the center channel velocity and the two bordering channel velocities for *Case 1* is about 6.5 ft/s and for *Case 4* it is about 7.0 ft/s making a difference between the two *cases* about 0.5 ft/s.
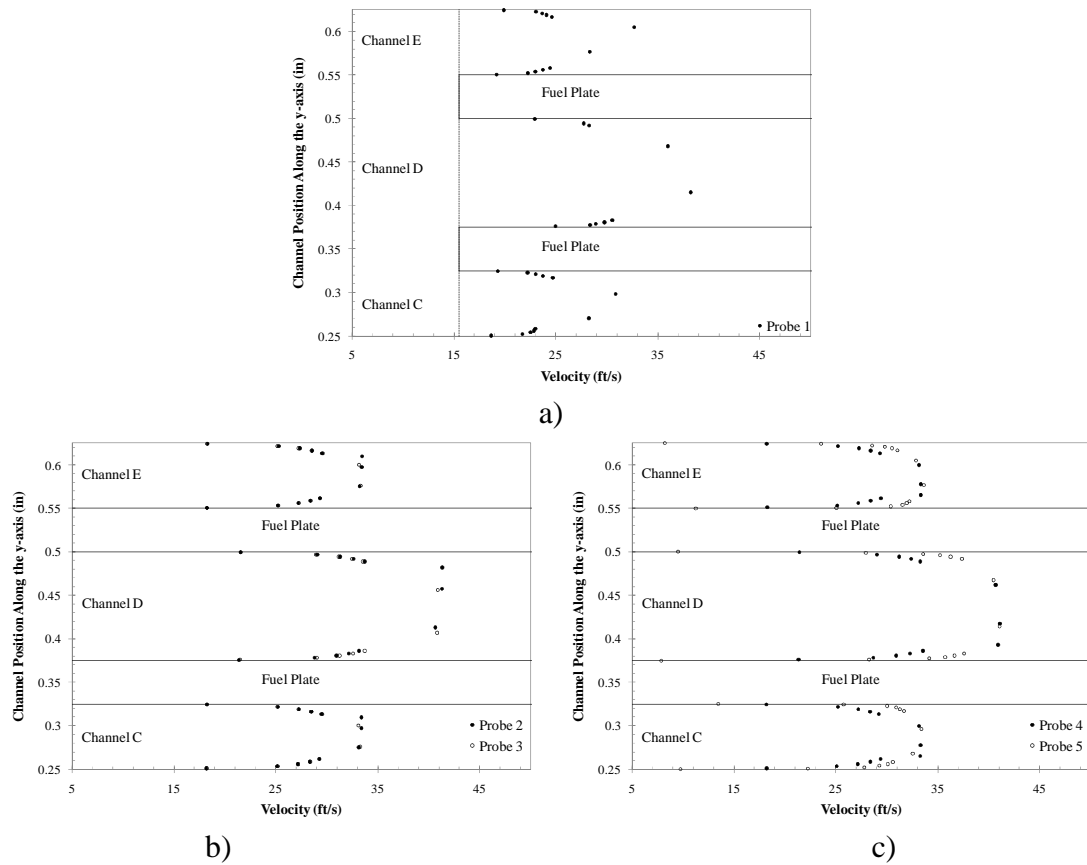
Figure 4.31: Case 4 velocity profiles for a) Probe 1, b) Probes 2 and 3, and c) Probes 4 and 5

Figure 4.31 also shows that the velocity in *Case 4* is faster than the velocity in *Case 1* again with the center channel being faster than the two outer channels and the velocity for Probe 1 being not yet fully developed.

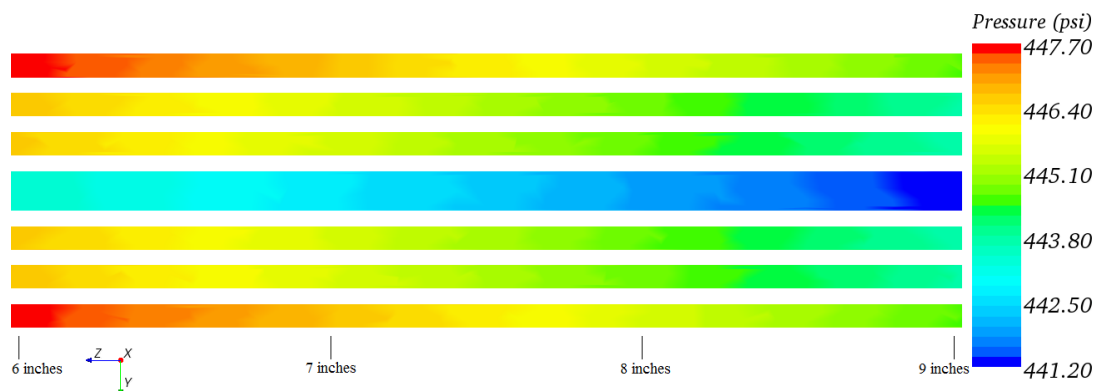The pressure profile for *Case 4* is shown in Figure 4.32.

Figure 4.32: Case 4 pressure profile for all seven channels

Again the same behavior is observed with the center channel having a lower overall pressure than the other six channels and that the two outermost channels have a higher velocity at a given location than the others. It is important to note that the scale on Figure 4.32 has a maximum pressure that is 5 psi higher than the scale in Figure 4.28. This is a result of the increased flow rate causing an increase in overall pressure.

### 4.3.3 Case 7

The flow rate again was changed for *Case 7* from 12.7 kg/s, which was the flow rate in *Case 4,* to 14.3 kg/s as a result of the increased volumetric flow rate. This again caused a similar increase in both pressure and velocity as will be shown in the following figures.

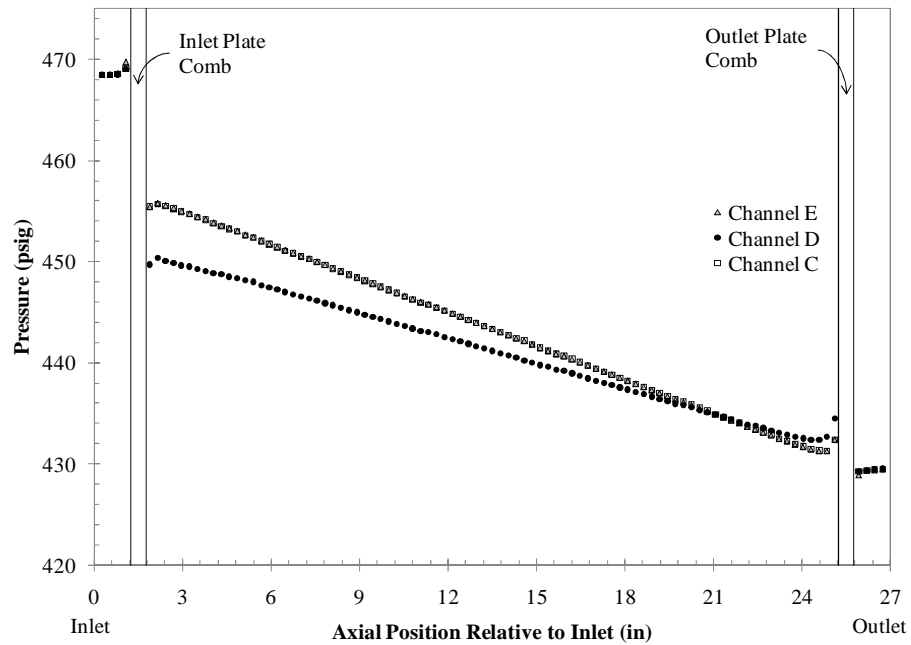Figure 4.33 shows the pressure drop through the three center channels.

Figure 4.33: Case 7 pressure drop through the three center channels

There is again a noticeable increase in inlet pressure from the previous *case*. Also the difference between the pressures after entering the channel is about 1 psig higher than it was in *Case 4* which means it is about 2 psig higher than it was in *Case 1*. This gives strong indication that fuel plates are more likely to deflect with an increase in the flow rate.

The velocity plots again show that with an increase in volumetric flow rate the velocity also increases. The plot of the velocities along the Middle Middle line probe is shown in Figure 4.34.
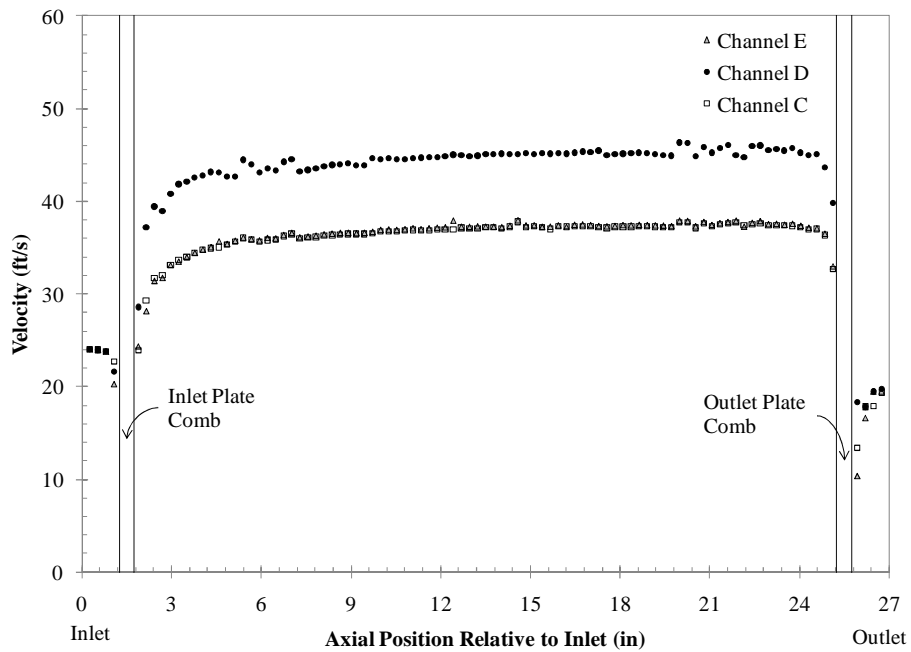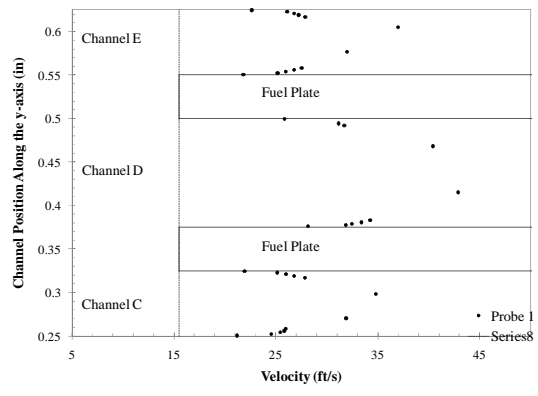
Figure 4.34: Case 7 velocity through the three center channels

The difference between the overall center channel velocity and the velocity through the two side channels is about 7.8 ft/s. This is about 0.8 ft/s more than in *Case 4* and about 1.3 ft/s more than in *Case 1*.

Figure 4.35 shows the plots generated using the velocity profile probes from Figure 3.4.

a)
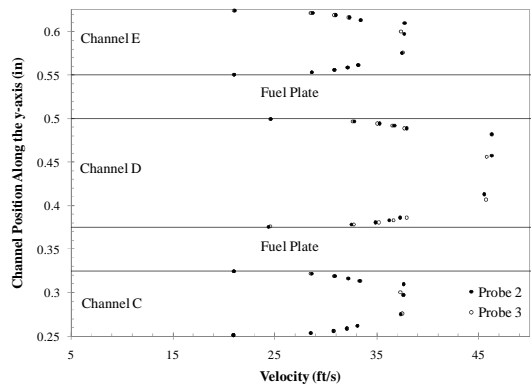


b)
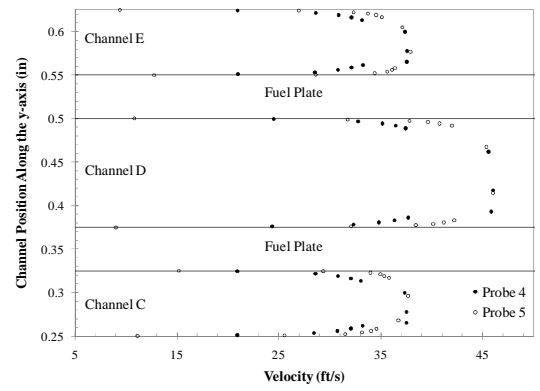


c)

Figure 4.35: Case 7 velocity profiles for a) Probe 1, b) Probes 2 and 3, and c) Probes 4 and 5

The same behavior is observed for *Case 7* as was observed for the previous two cases with an increase in the overall velocity in each channel.

The pressure profile for all seven channels is given in Figure 4.36.
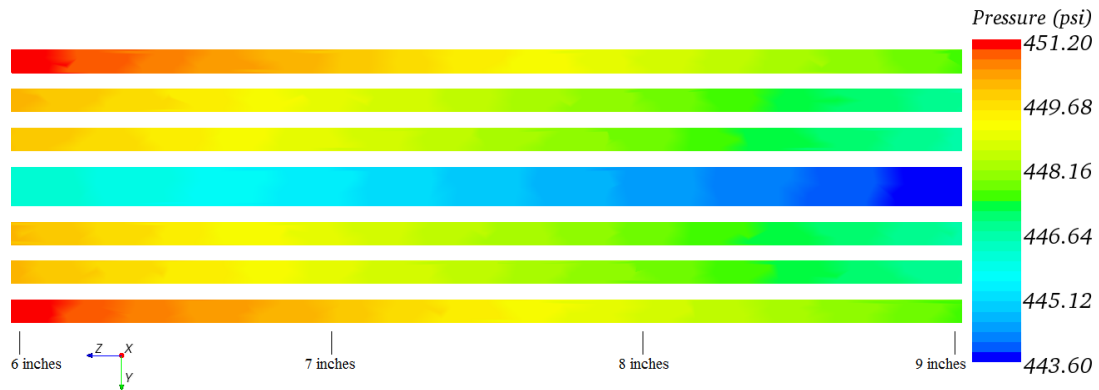
Figure 4.36: Case 7 pressure profile for all seven channels

The behavior is similar to the previous *cases* noticing again that with this increased flow rate the maximum pressure value on the scale was increased by another 5 psi in order to accommodate the increase in pressure.

### 4.3.4  Case 8

The next two *cases* have the same volumetric flow rate as *Case 7*. However, these next two *cases* have an increase temperature and because of the increase in temperature the density of the water is changed causing the mass flow rate for these two cases to be different than the mass flow rate for *Case 7* even though the volumetric flow rate remains the same.

The pressure plots along the Middle Middle line probe are given in Figure 4.37.
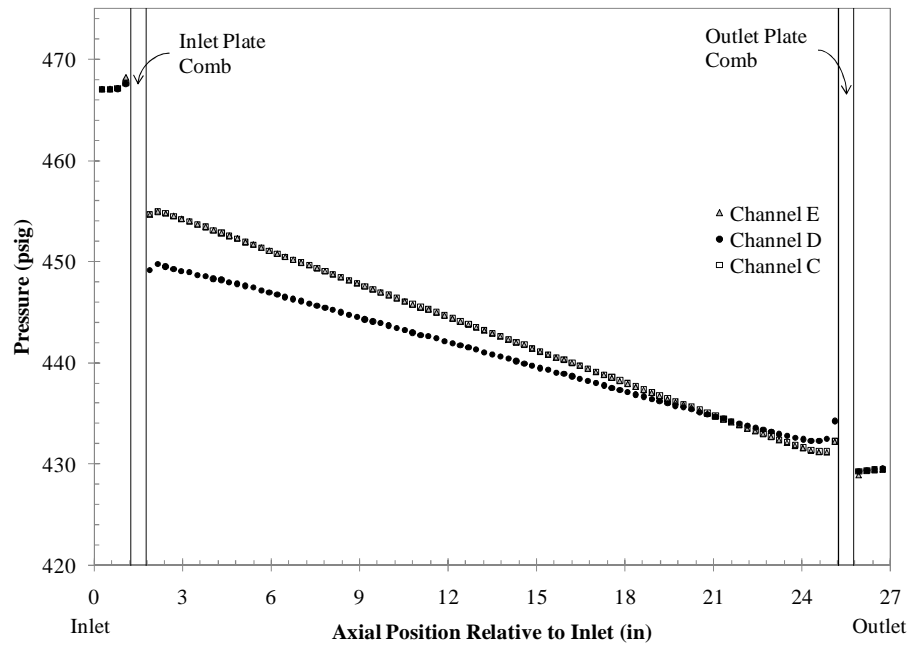
Figure 4.37: Case 8 pressure drop through the three center channels

Figure 4.37 is very similar to Figure 4.33. The inlet pressure is slightly lower than it was for *Case 7* but the change is not nearly as significant as it was with the different volumetric flow rate.

The velocity plots along the Middle Middle line probe are shown in Figure 4.38.
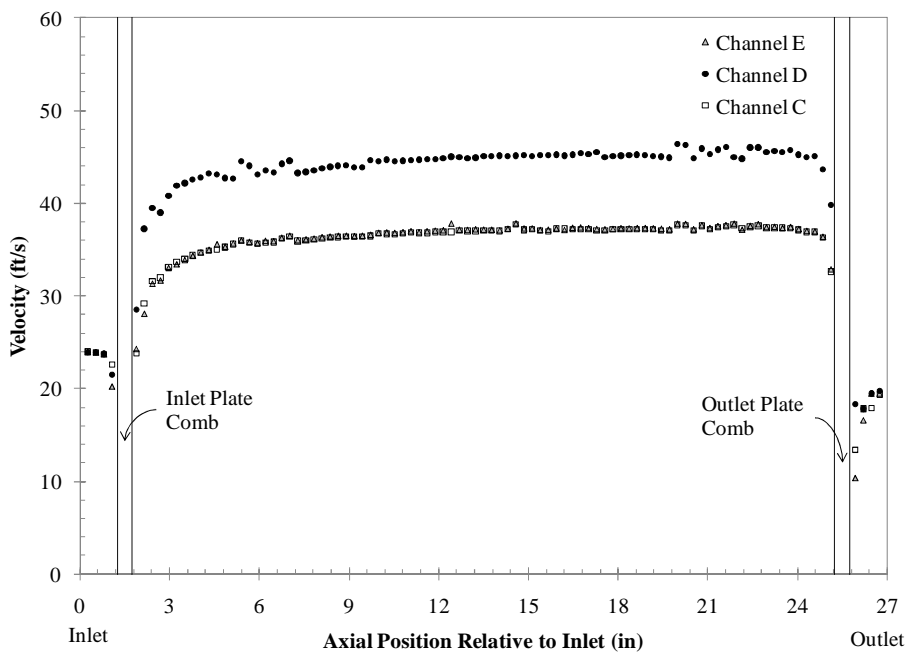
Figure 4.38: Case 8 velocity through the three center channels

The velocity also decreases slightly as a result of the increase in temperature and decrease in fluid density. This change is also not as large as the change associated with the volumetric flow rate change.

The plots from the velocity probes are shown in Figure 4.39.
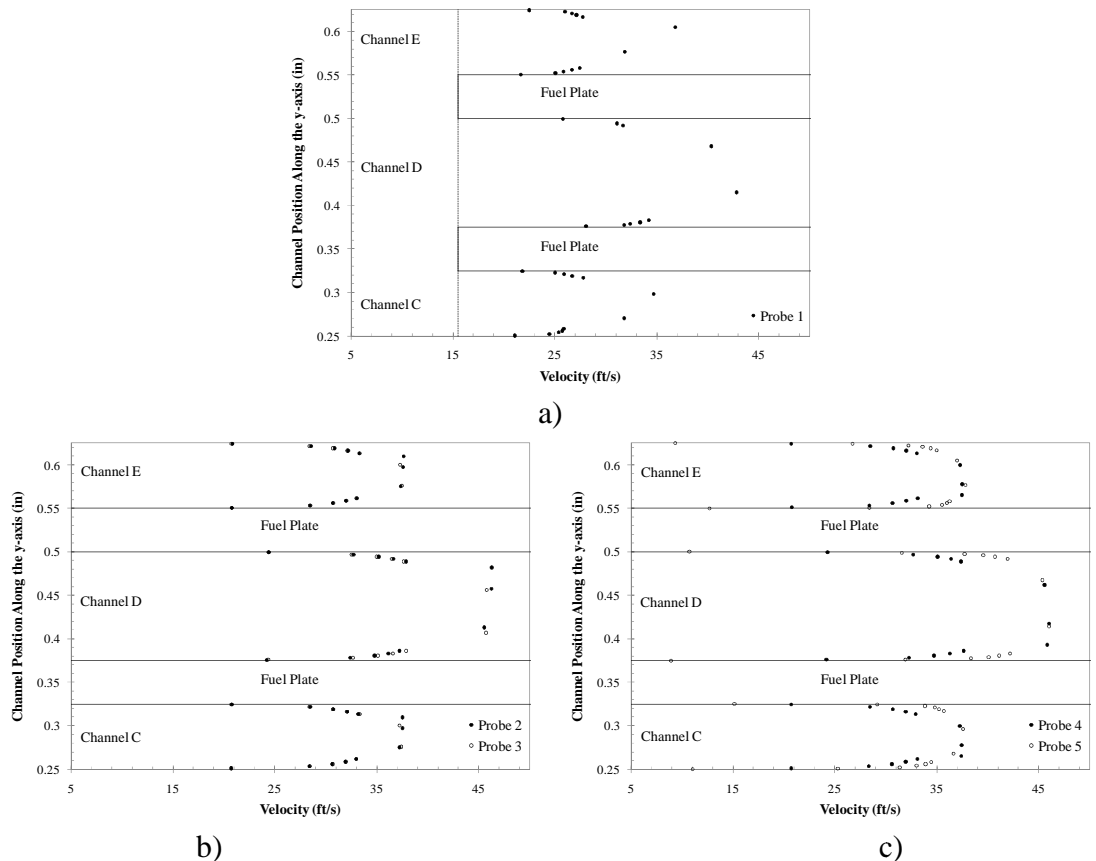
Figure 4.39: Case 8 velocity profiles for a) Probe 1, b) Probes 2 and 3, and c) Probes 4 and 5

The view graph showing the profile of the pressure in the full seven channel model is shown in Figure 4.40.
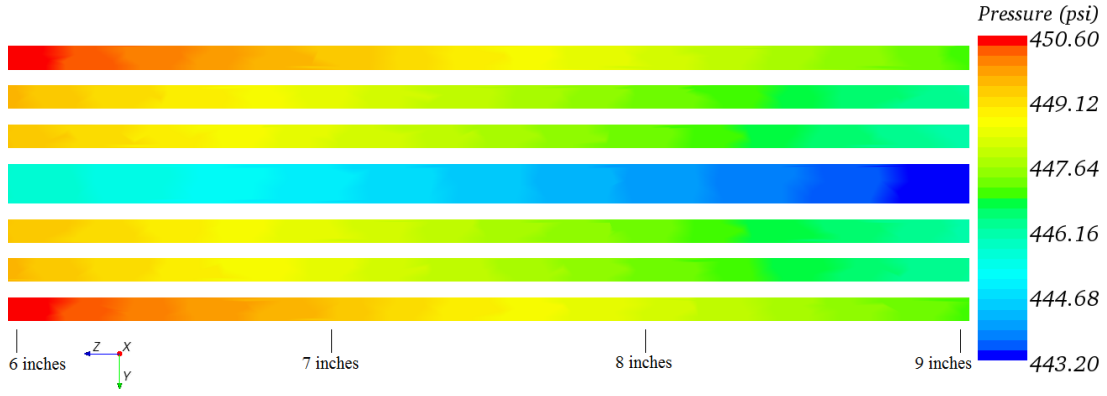


Figure 4.40: Case 8 pressure profile for all seven channels

Each figure indicates that there is not much difference between the results from *Case 7* and the results from *Case 8*.

### 4.3.5  Case 9

The temperature increase from *Case 7* to *Case 8* was larger than the temperature increase from *Case 8* to *Case 9* therefore, similar behavior is expected.

The pressure plots along the Middle Middle line probe are shown in Figure 4.41.
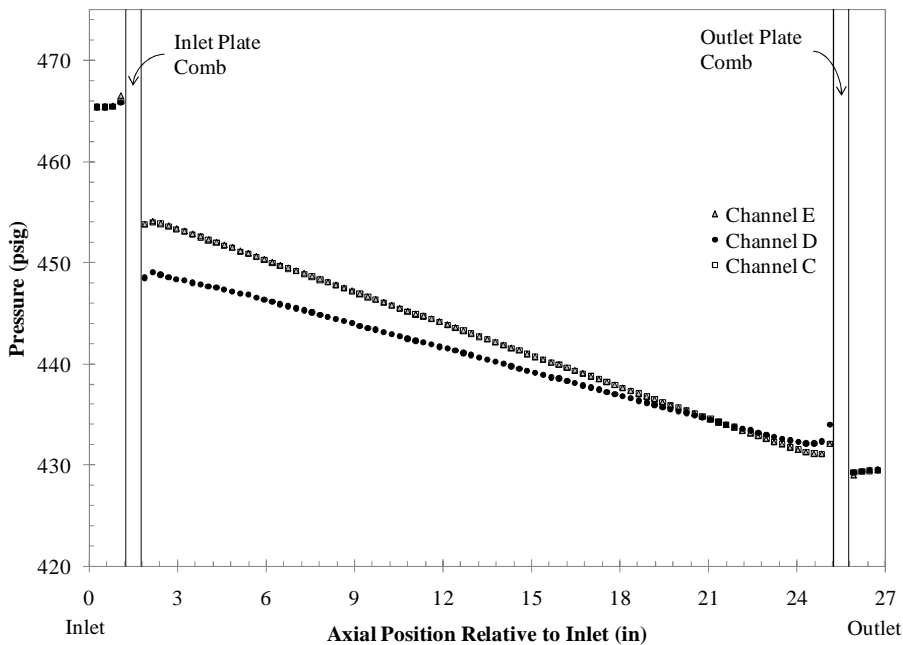


Figure 4.41: Case 9 pressure drop through the three center channels

Again the pressure is slightly lower at the inlet than the inlet pressure of *Case 8*.

The velocity plots along the Middle Middle line probe are given in Figure 4.42.
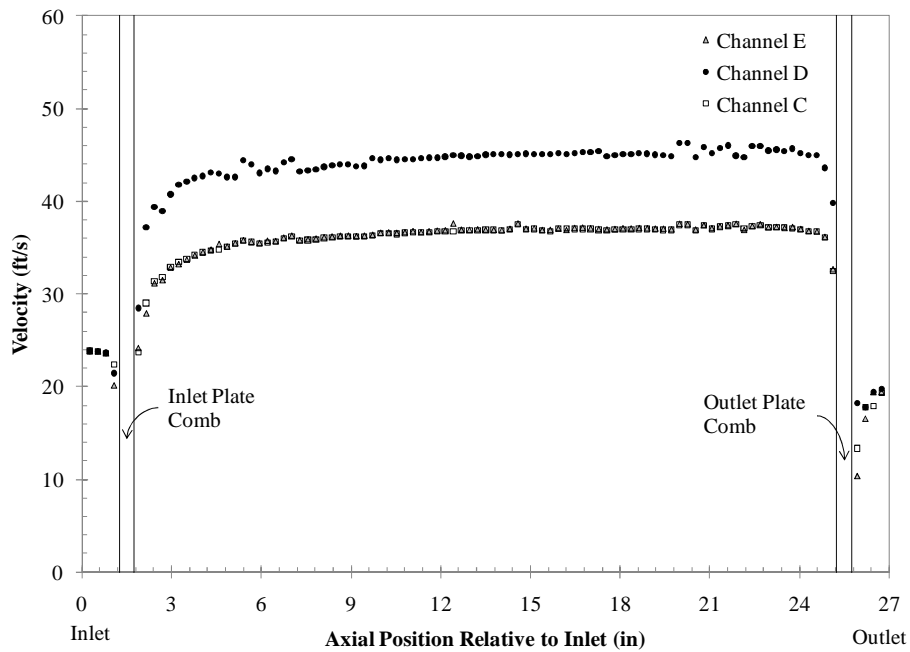
Figure 4.42: Case 9 velocity through the three center channels

The velocity is a bit lower than the velocity presented in *Case 8*. Even though these changes are not as large as the changes caused by the increase in volumetric flow rate they are still significant changes.

The velocity collected from the five velocity profile probes is given in Figure 4.43.
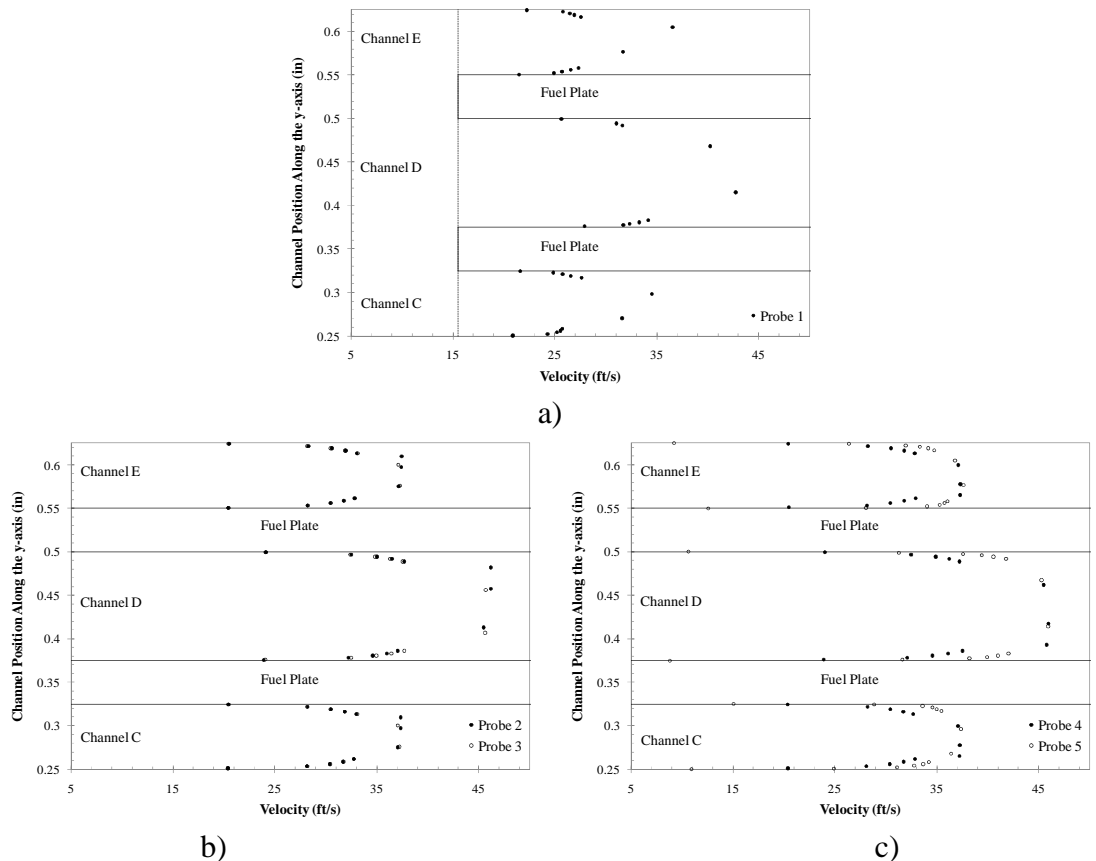
Figure 4.43: Case 9 velocity profiles for a) Probe 1, b) Probes 2 and 3, and c) Probes 4 and 5

Figure 4.43 shows similar behavior as the previous velocity profile graphs and also shows a similar increase in velocity as a result of the change in temperature.

The profile of the pressure through the full model is shown in Figure 4.44. Again, the changes from *Case 8* are noticeable but not very severe.
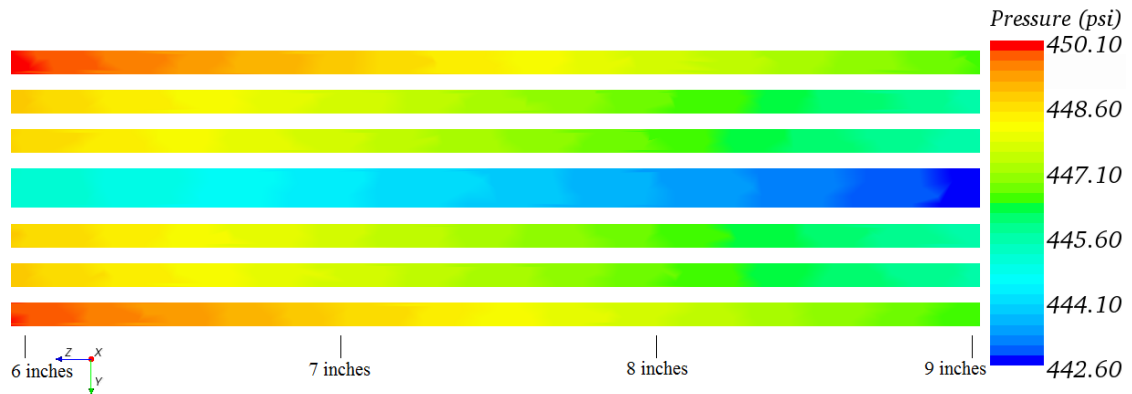
Figure 4.44: Case 9 pressure profile for all seven channels

## 4.3.6 Case Comparisons

The pressure and velocity data were used to distinguish the changes that occurred as a result of the different boundary conditions applied in each *case*. The six additional line probes shown in Figure 3.8 were used to collect this data.

The velocity was measured along each of the six additional line probes and the data was used to compare with values obtained using Miller's critical velocity equation shown in Equation (3.7). The location at which the critical velocity equation applies is at the inlet of the channel and along the same axial distance as the support comb. Therefore, only the velocity in this region was used for the comparison. Taking an average of the velocity in the support comb region yielded one value associated with each line probe, meaning two values in each channel. These two values were also averaged giving one value for each channel. This was done for each of the five cases. These values are shown in Table 4.5.

Table 4.5: Pressure and velocity data for Channels C, D, and E

| Variable | Case 1 | Case 4 | Case 7 | Case 8 | Case 9 |
|---|---|---|---|---|---|
| Channel E Average Velocity (ft/s) | 24.56 | 27.82 | 31.35 | 31.28 | 31.13 |
| Channel D Average Velocity (ft/s) | 31.06 | 34.99 | 39.21 | 39.21 | 39.13 |
| Channel C Average Velocity (ft/s) | 24.34 | 27.59 | 31.08 | 31.02 | 30.86 |

As has been shown previously, the velocity in Channels C and E match closely in each case. One important trend to take note of is that the velocity increases significantly when the volumetric flow rate changes from *Case 1* to *Case 7* but then decreases slightly as the temperature increases from *Case 7* to *Case 9*.

The values for critical velocity for each channel were calculated using Equation (3.7) and are given in Table 4.6.

Table 4.6: Miller's critical velocities for each case

| Channel | Case 1 | Case 4 | Case 7 | Case 8 | Case 9 |
|---|---|---|---|---|---|
| 0.125 inch Channel Critical Velocity (ft/s) | 100.23 | 100.23 | 100.23 | 102.65 | 105.58 |
| 0.075 inch Channel Critical Velocity (ft/s) | 77.64 | 77.64 | 77.64 | 79.51 | 81.78 |

The values for critical velocity are much higher than the calculated values. This indicates that there will be no measurable deflection at the inlet of the channel. The reason the critical velocity is so high is because this region has been stiffened by the addition of the support comb.

The net pressure across the plate behaves in a similar manner to the velocity in that the maximum net pressure increases with increasing velocity and decreases with increasing temperature. Line probes CC 1 and CC 2 were used to collect the required pressure data. Only these two probes were used because previous data indicates that the flow is symmetric around the center channel and also around the support comb. The difference in pressure from these two probes was calculated and the plot including each of the five cases is shown in Figure 4.45.
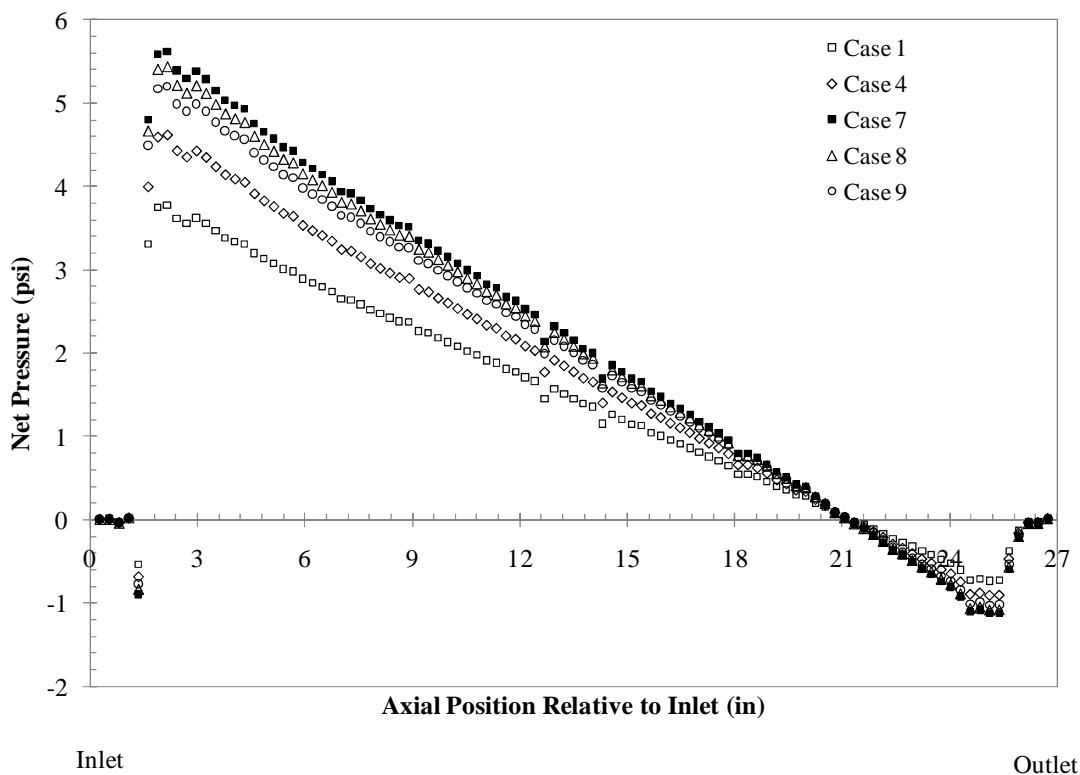
Figure 4.45: Net pressure on center channel plate for each *case*

This figure indicates that for each case the net pressure is highest as the fluid enters the fueled region with the net pressure in *Case 7* being higher than any other *case*. This figure also indicates that there is a more significant change associated with increasing volumetric flow rate than there is with increasing temperature. Even though the largest net pressure at the inlet of the fueled region the previous velocity data indicates that there will be no deflection in that region.

## *4.3.7 Material Differences*

As was mentioned in Section 1.1 the three materials used for the fuel plates will have different material properties. The ATR SAR indicates that the aluminum plate provides a more conservative estimate for deflection than the U-Al$_x$ dispersion fuel. The monolithic fuel can be analyzed using a rule-of mixtures estimate to determine the Young's modulus for the material. This equation is given below.

$$E_T = v_f E_f + v_m E_m \tag{4.1}$$

Where $E_T$ is the total Young's modulus for the plate, $v_f$ is the volume fraction of the fuel, $E_f$ is Young's modulus for the fuel, $v_m$ is the volume fraction of the matrix, and $E_m$ is Young's modulus for the matrix. The value for Young's modulus for Al-6061, the material used for the matrix, is $10.0 \times 10^6$ psi [38].

First, Young's modulus for the DU-Mo alloy is obtained using Equation (4.1). The weight percent of molybdenum is 10 percent which leads to a volume percent of 17.2 percent. The Young's modulus for depleted uranium, which is the same as it is for uranium, is 208 GPa [39]. The Young's modulus for molybdenum is 329 GPa [39]. This gives a Young's modulus for the DU-Mo alloy of 228.8 GPa which is equal to 33.2 psi.

The volume fractions for the fuel foil and the matrix can be obtained using the geometry given in the design of the GTPA fuel plate [18]. The fueled region is 23 inches by 3.5 inches. The total plate thickness is 0.05 inches and the fuel foil is 0.02 inches. This means that $v_f$ has a value of 0.4 and $v_m$ a value of 0.6. Therefore the value for the effective Young's modulus in the fueled portion of the plate is $19.28 \times 10^6$ psi.

Therefore, the higher modulus of elasticity indicates that the DU-Mo plate will be less likely to deflect than the pure aluminum plate. This indicates that the results from the pure aluminum plate would give a conservative estimate of when plate deflection is expected to occur.

# 5 CONCLUSIONS AND FUTURE WORK

## 5.1 Conclusions

Using the one channel model to select the criteria that would be used in the seven channel model proved effective. This method reduced the amount of time required to select the mesh type, turbulence model approach, and mesh size.

The two channel model helped to ensure that the criteria selected in the one channel model would continue to function with no obvious issue in the solution as a result of the more complex geometry. It was also useful to observe differences in the flow caused by an asymmetric geometry.

The different *cases* analyzed in the seven channel model gave ample evidence of the affect that varying boundary conditions have on the pressure differential within the GTPA. These results showed that the pressure differential between the channels becomes larger as the volumetric flow rate increases over a range of 179 gallons per minute to 229 gallons per minute. The results also showed that as the temperature increased from 120 °F to 350 °F the pressure differential between the channels decreased.

Comparing these results to Miller's critical velocity shows that the presence of the support comb is sufficient to stiffen the leading edge and prevent plate deflection in this location. However, this does not mean that deflection will not occur further down the plate. Further analysis should be done to determine if these results will contribute to plate deflection in other regions of the assembly.

The data produced using Star-CCM+ seems to reflect expected flow patterns. However, in order to verify that the results are an accurate representation of actual fluid flow they must be verified by experimental data. These comparisons will be made when experimental data from the HMFTF is obtained.

## 5.2 Future Work

This data supported some assumptions relating to the HMFTF in that the support comb will prevent the leading edge from experiencing deflection. However, it is necessary to use another program to input the results from this study to determine the locations that are most likely to experience deflection.

The k-ε approach needs to be analyzed using the percent difference method for RL 6 to determine if it could, in fact, be used in place of the RSM approach. If so then future simulations could use the k-ε approach and save on computation time.

The next step in the HMFTF project as a whole is to obtain experimental data using the facility that is currently under construction at OSU. The boundary conditions required to cause plate deflection will be used in additional CFD simulations. The experimental results will then be compared to the CFD results in an attempt to validate Star-CCM+ for this application. If the results are similar then Star-CCM+ can be used for future analysis as an accurate representation of actual fluid flow.

# 6   REFERENCES

1. IAEA. *Research Reactors*. 2009 [cited 2011 10 May 2011]; Available from: http://nucleus.iaea.org/RRDB/RR/ReactorSearch.aspx?rf=1.

2. Wiest, J.D., W.R. Marcum, and A.M. Phillips, *Hydro Mechanical Fuel Test Facility (HMFTF) Generic Test Plate Assembly (GTPA) Test*. 2011, Idaho National Laboratory: Idaho Falls, Idaho.

3. SAR-153, *Upgraded Final Safety Analysis Report for the Advanced Test Reactor.* Chapter 4, Revision 9, 10 Aug, 2004.

4. Marcum, W.R., et al., *The OSU Hydro-Mechanical Fuel Test Facility: Standard Fuel Element Testing*, in *RERTR 2010-32nd International Meeting on Reduced Enrichment for Research and Test Reactors*. 2010: Lisbon, Portugal.

5. Miller, D.R., *Critical Flow Velocities for Collapse of Reactor Parallel-Plate Fuel Assemblies*. 1958, Knolls Atomic Power Laboratory. p. 1-25.

6. Smissaert, G.E., *Static and Dynamic Hydroelastic Instabilities in MTR-Type Fuel Elements Part I. Introduction and Experimental Investigation.* Nuclear Engineering and Design, 1968. **7**: p. 535-546.

7. Smissaert, G.E., *Static and Dynamic Hydroelastic Instabilities in MTR-Type Fuel Elements Part II. Theoretical Investigation and Discussion.* Nuclear Engineering and Design, 1968. **9**: p. 105-122.

8. Ho, M., G. Hong, and A.N.F. Mack, *Experimental Investigation of Flow-Induced Vibration in a Parrallel Plate Reactor Fuel Assembly*, in *15th Australian Fluid Mechanics Conference*. 2004: The University of Sydney, Sydney, Australia.

9. Kane, J.J., *The Effect of Inlet Spacing Deviations on the Flow-Induced Deflections of Flat Plates.* Nuclear Science and Engineering, 1962. **15**: p. 305-308.

10. Groninger, R.D. and J.J. Kane, *Flow Induced Deflections of Parrallel Flat Plates.* Nuclear Science and Engineering, 1963. **16**: p. 218-226.

11. Ferris, H.D. and J.C. Moyers, *Advanced Test Reactor Fuel Element Hydraulic Buckling Tests*. 1963, The United States Atomic Energy Commission: Lynchburg, Virginia.

12. Rosenberg, G.S. and C.K. Youngdahl, *A Simplified Dynamic Model for the Vibration Frequencies and Critical Coolant Flow Velocities for REactor Parrallel Plate Fuel Assemblies.* Nuclear Science and Engineering, 1962. **13**: p. 91-102.

13. Johansson, E.B., *Hydraulic Instability of Reactor Parallel-Plate Fuel Assemblies.* 1959. p. 1-46.

14. Davis, D.C. and G. Kim, *Design Against Hydrodynamic Instabilities in Flat-Plate Type Fuel Element Assamblies.* The Pennsylvania State University, 1991: p. 105-109.

15. Davis, D.C. and G. Kim, *Hydrodynamic instabilities in flat-plate-type fuel assemblies.* Nuclear Engineering and Design, 1995. **158**: p. 1-17.

16. Guo, C.Q., R.H. Peng, and D.L. Sun, *A Dynamic Model for Flow-Induced Vibration of Parallel-Plate Fuel Assemblies.* Hengyang Institute of Technology, 1993: p. 1-4.

17. Smith, R.L., *Dynamic Pressure Limits for Flat Plates as Related to Nuclear Fuel Elements*, in *Nasa Technical Note*. 1968: Cleveland, OH. p. 1-30.

18. *Generic Test Plate Assembly - Fuel Plate Assembly.* Drawing Number 771770, Revision 1, November 8, 2010.

19. Yoo, S.H., et al., *Full-scope Simulation of a Dry Storage Cask uning Computational Fluid Dynamics.* Nuclear Engineering and Design, 2010.

20. Fletcher, D.F., M. McCaughey, and R.W. Hall, *Numerical simulation of a laminar jet flow: a comparison of three CFD models.* Computer Physics Communications, 1993. **78**: p. 113-120.

21. Krepper, E., B. Koncar, and Y. Egorov, *CFD modeling of subcooled boiling-Concept, validation and application to fuel assembly design.* Nuclear Engineering and Design, 2007. **237**: p. 716-731.

22. Liu, C.C. and Y.M. Ferng, *Numerically simulating the thermal-hydraulic characteristics within the fuel rod bundle using CFD methodology.* Nuclear Engineering and Design, 2010. **240**: p. 3078-3086.

23. Garland, W.J., *Thermalhdraulic Modeling of the McMaster Nuclear Reactor.* 1997, McMaster University: Hamilton, Ontario.

24. Hamman, K.D. and R.A. Berry, *A CFD simulation process for fast reactor fuel assemblies.* Nuclear Engineering and Design, 2010. **240**: p. 2304-2312.

25. Tan, K.K. and Y.W. Tan, *Simulations of Migration and Emissions of Gases in Sand-Cover of Landfill*, Universiti Putra Malaysia: Selangor, Darul Ehsan, Malaysia.

26. Tan, K.-K., Y.-W. Tan, and T.S.Y. Choong, *Onset of natural convection induced by bottom-up transient mass diffusion in porous media.* Powder Technology, 2009. **191**: p. 55-60.

27. Ha, T. and W.J. Garland, *Hydraulic study of turbulent flow in MTR-type nuclear fuel assembly.* Nuclear Engineering and Design, 2006. **236**: p. 975-984.

28. Srivastava, R.R., N.M. Schneider, and S.G. Kandlikar, *Numerical Simulation of Single Phase Liquid Flow in Narrow Rectangular Channels with Structured Roughness Walls*, in *ASME 2009 7th International Conference on Nanochannels, Microchannels and Minichannels*. 2009: Pohang, South Korea. p. 1-7.

29. Anglart, H., et al., *CFD prediction of flow and phase distribution in fuel assemblies with spacers.* Nuclear Engineering and Design, 1997. **177**: p. 215-228.

30. Koncar, B., E. Krepper, and Y. Egorov, *CFD Modeling of Subcooled Flow Boiling for Nuclear Engineering Applications*, in *Nuclear Energy for New Europe 2005*. 2005: Bled, Slovenia. p. 140.1-140.13.

31. Anglart, H. and O. Nylund, *CFD application to prediction of void distribution in two-phase bubbly flows in rod bundles.* Nuclear Engineering and Design, 1996. **163**: p. 81-98.

32. Conner, M.E., E. Baglietto, and A.M. Almahdi, *CFD methodology and validation for single-phase flow in PWR fuel assemblies.* Nuclear Engineering and Design, 2010. **240**: p. 2088-2095.

33. Calis, H.P.A., et al., *CFD modeling and experimental validation of pressure drop and flow profile in a novel structured catalytic reactor packing.* Chamical Engineering Science, 2001. **56**: p. 1713-1720.

34. *Star-CCM+ User's Guide.*

35. White, F.M., *Viscous Fluid Flow*. 3rd ed. 2005: McGraw-Hill.

36. Richardson, L.F., *The approximate arithmetical solution by finite differences of physical problems involving differential equations with an application to the stresses in a masonry dam.* . Trans. Roy. Soc. London, Ser. A, 1910. **210**: p. 307-357.

37. Ferziger, J.H., *Computational Methods for Fluid Dynamics*. 3rd ed. 2002, New York: Springer.

38. Boresi, A.P. and R.J. Schmidt, *Advanced Mechanics of Materials*. 6th ed. 2003: John Wiley & Sons, Inc.

39. Winter, M. *Web Elements*. 2010 [cited 2011; Available from: www.webelements.com.

40. Zeng, D. and G. Landgraf, *Vibration of Thick Plates with Damping*. 1987.

41. Wambsganss, M.W.J., *Second-Order Effects as Related to Critical Coolant Flow Velocities and Reactor Parallel Plate Fuel Assemblies*. Nuclear Engineering and Design, 1967. **5**: p. 268-276.

42. Petyt, M. and J.M.D. Nath, *Vibration Analysis of Singly Curved Rectangular Plates*. Journal of Sound Vibration, 1969. **13**(4): p. 485-497.

43. Guillen, D.P. and M.J. Russell, *Estimation of Critical Flow Velocity for Collapse of Gas Test Loop Booster Fuel Assembly*. 2005. p. 1-14.

44. Cui, Z.-D., et al., *Flow-induced vibration and stability of an element model for parallel-plate fuel assemblies*. Nuclear Engineering and Design, 2008. **238**: p. 1629-1635.